日本磁気学会
ISSN 2432-0250
Journal of the Magnetics Society of Japan
Electronic Journal URL: https://www.jstage.jst.go.jp/browse/msjmag

Vol.41 No.6　2017

Journal

Review Article

Development of Media Nanostructure for Perpendicular Magnetic Recording

M. Futamoto and M. Ohtake…108

Hard and Soft Magnetic Materials

Synthesis and Magnetic Properties of ($Zn^{2+}Ti^{4+}$) Substituted W-type and Y-type Ferrites

K. Watanabe, K. Kakizaki, and K. Kamishima…127

Power Magnetics

Low Permeability Composite Magnetic Core Transformer with High Coupling Coefficient and its Application to PFM Controlled Quasi-Resonant Mode Flyback-Type DC-DC Converter

K. Sato, T. Sato, M. Sonehara, and H. Takeuchi…132

広告　◇東英工業株式会社　◇計測エンジニアリングシステム株式会社　◇ネオアーク株式会社　◇TDK株式会社

JOURNAL OF THE MAGNETICS SOCIETY OF JAPAN

Vol.41 No.6 2017

日本磁気学会

ISSN 2432-0250

HP: http://www.magnetics.jp/ e-mail: msj@bj.wakwak.com
Electronic Journal: http://www.jstage.jst.go.jp/browse/msjmag

世界初！
高温超電導型VSM

新製品

世界初*、高温超電導マグネットをVSMに採用することで
測定速度 当社従来機1/20を実現。
0.5mm cube磁石のBr, HcJ高精度測定が可能と
なりました。

*2014年7月 東英工業調べ

測定結果例

高温超電導VSMによるNdFeB(sint.) 0.5mm cube BHカーブ

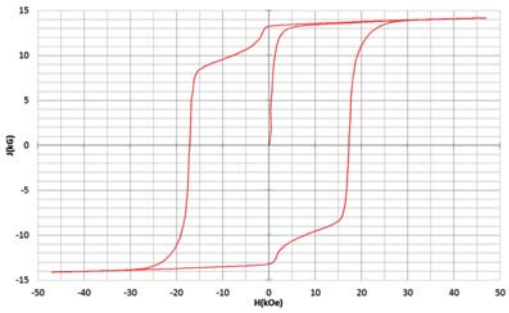

磁化測定レンジ：0.2emu
Br = 13.2kG　　HcJ = 17.2kOe

高温超電導VSMによるNdFeB(sint.) 1mm cube BHカーブ

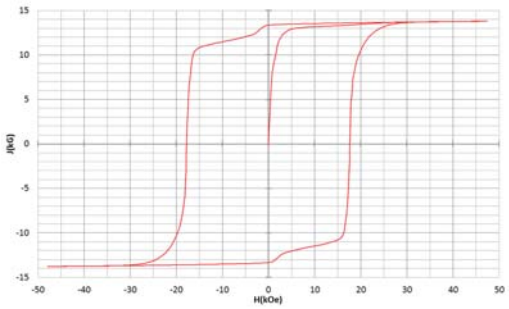

磁化測定レンジ：2emu
Br = 13.3kG　　HcJ = 17.7kOe

高温超電導VSMによるNdFeB(sint.) 4mm cube BHカーブ

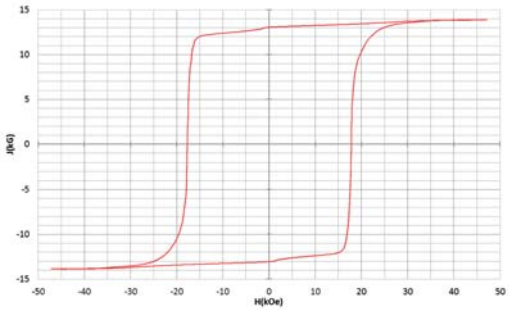

磁化測定レンジ：100emu
Br = 13.1kG　　HcJ = 17.8kOe

高速測定を実現

高温超電導マグネット採用により、高速測定を実現しました。Hmax= 5Tesla, Full Loop 測定が2分で可能です。
（当社従来機：Full Loop測定 40分）

小試料のBr,HcJ高精度測定

0.5mm cube 磁石のBr,HcJ 高精度測定ができ、表面改質領域を切り出しBr,HcJの強度分布等、微小変化量の比較測定が可能です。
また、試料の加工劣化の比較測定が可能です。

試料温度可変測定

−50℃～+200℃温度可変UNIT（オプション）

磁界発生部の小型化

マグネットシステム部寸法：0.8m×0.3m×0.3m

TOEI 東英工業株式会社
http://www.toeikogyo.co.jp

〒194-0035 東京都町田市忠生1-8-13
TEL：042-791-1211 FAX：042-792-0490
E-mail : sales@toeikogyo.co.jp

有限要素法解析ソフトウェア COMSOL Multiphysics®

COMSOL MULTIPHYSICS®

マルチフィジックスの進化論

無制限・強連成で実現象に即したシミュレーション事例のご紹介

永久磁石を利用した磁気軸受の解析例

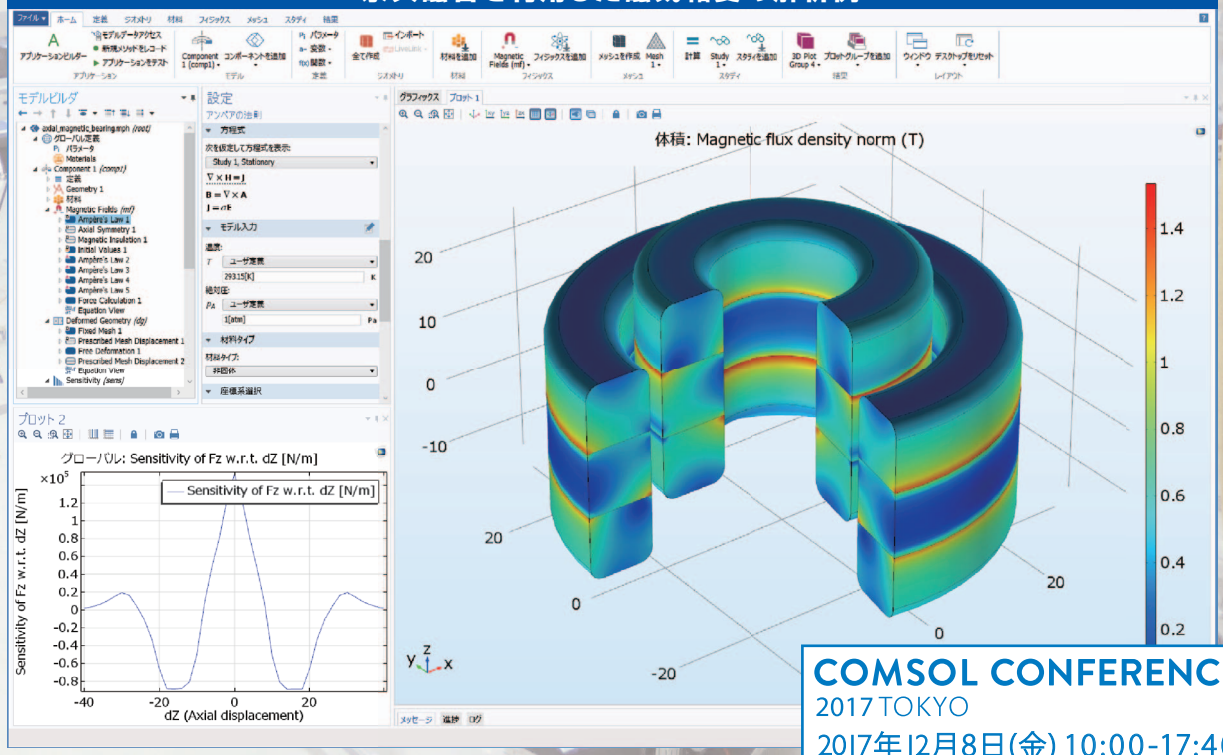

COMSOL CONFERENCE
2017 TOKYO
2017年12月8日(金) 10:00-17:40
秋葉原UDXビル4F (UDX Gallery/Next)
http://www.kesco.co.jp/conference/

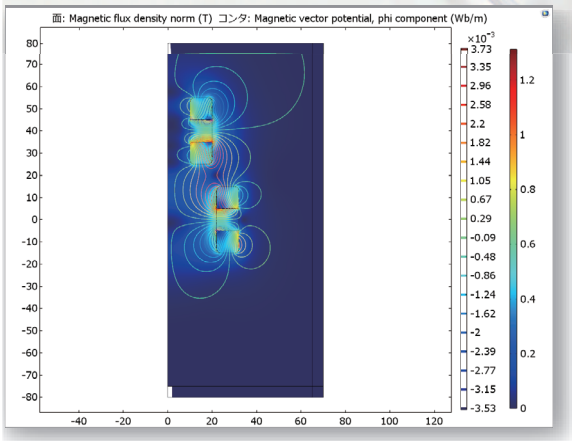

永久磁石を使用した磁気軸受

永久磁石を使用した軸受はターボ機械、ポンプ、モータ、発電機やフライホイール式エネルギー貯蔵システムなど、様々な分野で使用されています。非接触かつ潤滑不要で保守整備を大幅に省略できる点は、従来の機械式ベアリングと比べて重要なメリットです。
この例では、軸方向の永久磁石軸受の磁気力と剛性などの設計パラメータを計算する方法を示しています。

※AC/DCモジュールはCOMSOL Multiphysicsと併用するアドオン製品です。

AC/DC モジュールの適用例

- AC/DC 電流分布、電場分布
- バイオヒーティング
- コイルとソレノイド
- SPICE 回路とフィールドシミュレーション
- 接触抵抗
- 電磁両立性 (EMC) および電磁妨害 (EMI)
- 電磁力およびトルク
- 電磁力シールド
- 電気機械の変形
- ホール効果を利用したセンサ
- インシュレータ、コンデンサ、誘電体
- モータ、ジェネレータ、および他の電気機械
- 非線形材料
- 寄生容量とインダクタンス
- 永久磁石と電磁石
- 多孔質材料
- 抵抗および誘導加熱
- センサ
- 超伝導体
- 変圧器とインダクタ

COMSOL Multiphysics® なら、今まで不可能だった3種以上のマルチフィジックス解析を強連成で実現できます。30日間全機能無料トライアル、無料の導入セミナー、1000種を超える世界の様々な事例をご提供いたします。詳しくは、下記の弊社営業部までお問い合せください。

COMSOL
http://www.comsol.jp

KESCO KEISOKU ENGINEERING SYSTEM
計測エンジニアリングシステム株式会社
http://www.kesco.co.jp/comsol/
Tel : 03-5282-7040 ・ Fax : 03-5282-0808

COMSOL, COMSOL Multiphysics, COMSOL Desktop, COMSOL Server, LiveLinkはCOMSOL ABの商標または登録商標です。その他の製品名、サービス名、組織名は各組織の商標または登録商標です。

新型 磁区観察顕微鏡 シリーズ

小型磁区観察顕微鏡

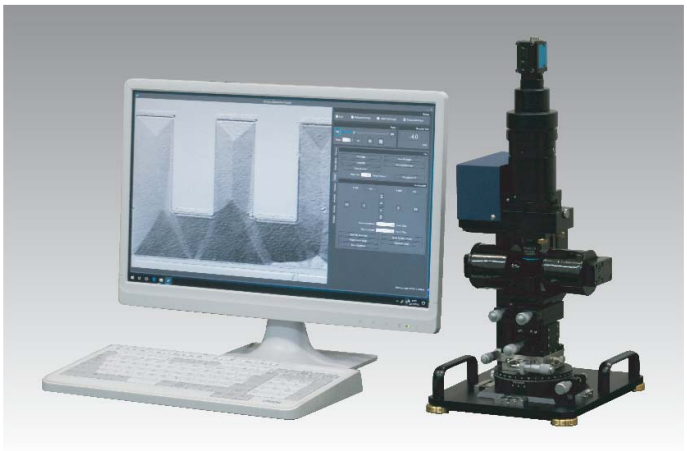

Neomagnesia Lite

※概要・特長

- 磁区観察ユニットに電磁石、 ステージ、 励磁電源、ソフトウェアを組み合わせたトータルシステム
- 従来の弊社の磁区観察顕微鏡から大幅なプライスダウンを実現
- 磁区の動的な観察を可能とする高機能な専用ソフトウェアが付属
- 最大で 1kOe（面内方向）の磁場を印加可能
- 本体の大きさは 210×260×475mm^3、 質量も 8kg と軽量・コンパクト
- 白色 LED 光源の採用により高安定・長寿命

磁区観察ユニット

※概要・特長

- プローバ装置などに取り付けることが可能な小型・低価格の磁区観察ユニット
- 面内 / 垂直どちらの磁化方向にも対応
- 社内設計光学系による面内磁区の高コントラスト観察（空間分解能 3μm 以下 ）
- 光学系ヘッドの大きさは 150×150×300mm^3、質量も 2kg と軽量・コンパクト
- 白色 LED 光源の採用により高安定・長寿命
- オプションとして顕微鏡スタンド・ステージ・高機能観察 / 解析ソフトウェアなどを用意

この製品以外に、 30 年の研究現場への対応経験に基づいた高精度・高性能の磁気 Kerr 効果装置、Faraday 装置、 磁区観察顕微鏡など、 各種磁気光学製品の取り揃えがございます。
お気軽にお問合せください。

レーザとレーザ応用システム製品の総合メーカー
NEOARK ネオアーク株式会社
営 業 部／〒156-0041 東京都世田谷区大原2-17-6-108 TEL(03)6379-5539 FAX(03)6379-5688
大阪支店／〒541-0056 大阪市中央区久太郎町2-3-8-201 TEL(06)6271-5123 FAX(06)6271-5110
本社 第1工場・第2工場／八王子市
URL http://www.neoark.co.jp E-mail:info@neoark.co.jp

Physicist
Peter Grünberg
未来をどこまで想像できるか。
進みつづける時間の先に、何を見るか。
止まることのない時間の向こうに、何を思い描くか。
想像したことのない未来は、創造できない。
まっすぐな視線の先にしか、新しい常識は現れない。
先駆的なアイデアだって、革新的なテクノロジーだって、
それは、未来を自由に想像し、未来を強く渇望し、
そこに向かおうとするひたむきな意志からしか生まれない。
未来とは、前を向く者だけに与えられる、
現在という時間からのかけがえのない贈り物だ。
だから、未来に夢を見よう。未来に絵を描こう。
この世界の未来を、どこまでも想像しよう。
www.attractingtomorrow.tdk.co.jp
Attracting Tomorrow
TDK

Journal of the Magnetics Society of Japan
Vol. 41, No. 6

Electronic Journal URL: https://www.jstage.jst.go.jp/browse/msjmag

CONTENTS

Review Article

Development of Media Nanostructure for Perpendicular Magnetic Recording
..... M. Futamoto and M. Ohtake 108

Hard and Soft Magnetic Materials

Synthesis and Magnetic Properties of ($Zn^{2+}Ti^{4+}$) Substituted W-type and Y-type Ferrites
..... K. Watanabe, K. Kakizaki, and K. Kamishima 127

Power Magnetics

Low Permeability Composite Magnetic Core Transformer with High Coupling Coefficient and its Application to PFM Controlled Quasi-Resonant Mode Flyback-Type DC-DC Converter
..... K. Sato, T. Sato, M. Sonehara, and H. Takeuchi 132

Board of Directors of The Magnetics Society of Japan

President:	K. Takanashi
Vice President:	K. Nakagawa, S. Nakamura
Director, General Affairs:	Y. Miyamoto, K. Niiduma
Director, Treasurer:	K. Aoshima, K. Ishiyama
Director, Planning:	Y. Saito, S. Nakagawa
Director, Editorial:	K. Kobayashi, T. Ono
Director, Public Relations:	H. Itoh, S. Greaves
Director, International Affairs:	Y. Takemura, M. Nakano
Auditor:	Y. Suzuki, R. Nakatani

J. Magn. Soc. Jpn., **41**, 108-126 (2017)

<Review>

Development of Media Nanostructure for Perpendicular Magnetic Recording

Masaaki Futamoto and Mitsuru Ohtake
Faculty of Science and Engineering, Chuo University, *1-13-27 Kasuga, Bunkyo-ku, Tokyo 112-8551, Japan*

The review covers the research and development of perpendicular media nanostructure focusing on the recording layer. The recording layer material includes the Co-alloys with hcp structure, the magnetic multilayers, and the alloys with ordered structures that have high magneto-crystalline anisotropies (K_u). The technologies of underlayer or interlayer for aligning the easy magnetization axis of magnetic crystal grain perpendicular to the film plane are briefly reviewed including the high K_u magnetic materials for future recording media.

Observations of compositional and magnetization structures in sub-μm scale have played important roles in improving the recording layer. Typical data on these characteristics are explained in relation to the media structure improvements. Considering that high K_u magnetic materials will be employed in future recording media, basic experimental results related in controlling the easy magnetization axis and in keeping the surface flatness of $L1_0$-ordered magnetic materials are explained. Future possibilities for increasing the areal density beyond 1 Tb/in^2 by improving the magnetic material and the nanostructure of recording layer are also discussed.

Key words: perpendicular magnetic recording, thin film media, nanostructure, compositional structure, magnetization structure, Co-alloy, ordered alloy, multilayer, high K_u magnetic material, epitaxial growth

1. Introduction

The areal density of hard disk drive (HDD) is now around 1 Tb/in^2 which is 5×10^8 of the areal density employed in the world-first HDD developed in 1956 (2 Kb/in^2, 100 bits/in, 20 tracks/in). Now all the HDDs are based on the perpendicular magnetic recording (PMR) technology that was invented by Prof. Iwasaki in 1976 [1]. PMR involves nearly 30 years of research and development before the technology started to be used in commercial HDDs in 2005 by replacing the conventional longitudinal magnetic recording (LMR) technology. Table 1 shows the brief history of research and development until the shipment of PMR-HDD, listed by keywords from a viewpoint of perpendicular magnetic recording media technology [2]. Although the PMR research and development attracted much attention in the magnetic recording community from late 1970's to early 1980's, there was a dip period of 10 - 15 years, from middle 1980's to late 1990's which is shown as the background shadow in the table, with low activities in the academic and the HDD-related communities. This was partially because that there were a couple of engineering issues [3-6] which needed to be solved before applying PMR to the commercial HDDs, and mainly due to that it was considered at that time possible to increase the areal density with the conventional LMR. The high cost for production facilities in changing the recording scheme could be an additional reason for the industries. However, as the areal density increased beyond 10 Gb/in^2, the signal decay problem associated with thermal instability with LMR [7-9] gradually narrowed the allowance in HDD product design. Triggered by a high-density magnetic recording demonstration using PMR[10] and by the developments of PMR media technology which solved the engineering issues[11-18], activities toward realization of HDD products based on PMR emerged drastically in the magnetic recording community from the year around 2000 and the first PMR-HDD product was shipped in 2005 with an areal density of 133 Gb/in^2 [19, 20]. The areal density of PMR-HDD increased since then about 10 times and the technologies for achieving 5 - 10 Tb/in^2 areal densities are investigated in the cutting edge research laboratories[21, 22].

In the PMR technologies, the recording media and the writing head are different from those for conventional LMR whereas other technologies like the reader head and the mechanical positioning have much in common. The present paper reviews the development of PMR media technology focusing on the nanostructure of Co-alloy recording layer. To further increase the areal density well beyond 1 Tb/in^2, magnetic materials with the magneto-crystalline anisotropy (K_u) higher than those of Co-alloys need to be employed. Some of the basic key points in tailoring the high K_u magnetic thin films are also briefly reviewed.

2. Technologies in controlling the structure of Co-alloy recording layer

When a CoCr-alloy magnetic material with hcp structure is deposited on a substrate, a texture growth proceeds with the *c*-axis direction perpendicular to the substrate surface[23], where the *c*-axis is the easy magnetization of Co-alloy crystal with an hcp structure. However, crystal grains with different growth orientations coexist in the early stage of film growth near the substrate as shown in the cross-sectional transmission electron microscope image of Fig.1 (a) [24].

Table 1 Research and development history of perpendicular magnetic recording media technologies [2)]

Year	1975	1980	1985	1990	1995	2000	2005	2010
Areal density	5 Mb/in^2	10 Mb/in^2		100 Mb/in^2	1 Gb/in^2	10 Gb/in^2	100 Gb/in^2	500 Gb/in^2
Recording layer	CoCr			CoCrTa	CoCrPt	CoPtCr + Oxides		
Technologies								
・Thin film media technology	**PMR invention by Prof. Iwasaki** (Tohoku Univ., 1976) CoCr-alloy PMR media (Tohoku Univ., 1978) SUL noise observation (Hitachi, 1984) *c*-axis control by underlayer (Hitachi, etc. 1985) PMR media, $L1_0$-FePt (AIT, 1997)				SUL noise reduction (JVC, 1996) Improved underlayers (Hitachi, 1996-1997) Media noise reduction (Hitachi, 1997-1998) High *Hc*, high *Mr/Ms* media (Hitachi, 1998) CoPtCrO high *Hc*, high *Mr/Ms* media (Toshiba, 2000) Improved SUL (Hitachi & many companies, 2000) CGC media (IBM & Tohoku Univ., 2002) Improved Ru-underlayer (Fujitsu, etc., 2005 -) PMR media, $SmCo_5$ (Shinshu Univ. Waseda Univ. etc., 2004)			
・Structure analysis technology	Cross-sectional TEM (Hitachi, etc., from around 1984) Segregation structure observation by TEM using chemically etched sample (NTT, 1984-1994) Magnetization structure observation by E-holography (Hitachi, 1986-1987) Magnetization structure observation by MFM (Hitachi, etc., from around 1992) Compositional segregation observation by AP-FIM (Tohoku Univ., 1992-1994) Compositional segregation observation by EELS and EDX TEM (Hitachi, from 1995) Basic magnetic properties determined using Co-alloy single-crystals, *Ku*, *α*, etc. (Hitachi, Tohoku Univ. from 1996)							
Events	Drastic growth of PMR R&D (Japan, US, Europe, 1976 - 1985)		Tribology-related problems, PMR-floppy-disk (Many companies, middle '80s) Pulling out from Ba-ferrite floppy PMR media business (Toshiba, late '80s) US HDD companies shifted to LMR, Japanese companies followed (middle-late '80s)	Giving-up PMR-HDD business (Censtor, Fujitsu,1991-1993) Negative report on PMR (IBM, 1998)	Thermal stability problem prediction (CMU, 1994)	52.5 Gb PMR demonstration (Hitachi, 2000)	Commercialization of PMR-HDDs (Toshiba, 2005)	

Areal density: the areal density of commercialized HDD and therefore the values before the year 2005 are those of LMR-HDDs.
Recoding layer: the typical recording layer material studied for PMR media. There were many variations, for example, CoCrPt*X* (*X*=Ta, Nb, Si, B, etc.).
Background shadow: it shows the R&D activities of PMR in the world. There was a dip period of 10 - 15 years from middle 80s to late 90s.

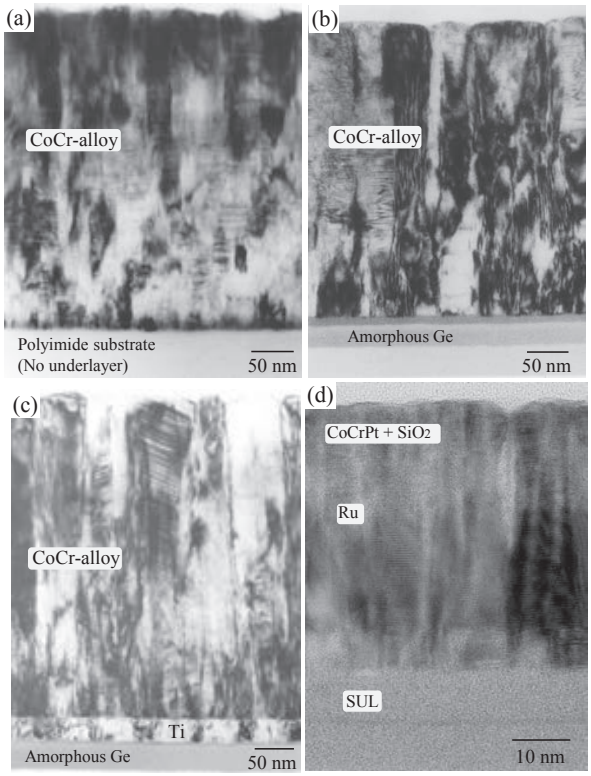

Fig. 1 TEM micrographs of PMR media [2)]. The numbers in parentheses are the years of observation or publication.
(a) CoCr-alloy thin film deposited on polyimide substrate with no underlayer, (1985). (b) CoCr-alloy thin film deposited on amorphous Ge underlayer, (1985). (c) CoCr-alloy thin film deposited on Ti/Ge composite underlayer, (1988). (d) CoCrPt + SiO_2 thin film deposited on Ru layer, (2008).

The presence of initial growth region is undesirable for PMR media, since it deteriorates the perpendicular magnetic anisotropy[25, 26)]. To enhance the crystal nucleation with the *c*-axis perpendicular to the substrate surface, underlayer materials were investigated around middle 1980's, and the materials like hcp-Ta [27)], hcp-Ti [28, 29)], amorphous-Ge [30)] were found suitable for this purpose. The underlayer has to offer a surface condition for Co-alloy crystal to nucleate with the basal (0001) parallel to the surface through hetero-epitaxial growth. Such nucleation of Co-alloy crystal is also possible on a neutral-type surface that promotes free nucleation of Co-crystal, where the (0001) basal plane with the lowest surface energy tends to be favored parallel to the nonmagnetic underlayer surface. Underlayer materials were then extended to nonmagnetic hcp-CoCr [31, 32)], hcp-Ru [30, 33)], fcc-Au, fcc-Al [34)], fcc-Pt [35)], etc. and dual-underlayer structures; Ti/Ge [36)], CoCr/TiCr [37, 38)], Co_3O_4/Pt [35)], Pt/Ti [39)], Pd/Ti [40)], CoCrRu/TiCr [41)], Ru/Ta [42, 43)], Ru-oxide/Ru [44)], etc. for the preparation of PMR media. Figures1 (a)-(d) show the variation in cross-sectional structure of CoCr-alloy film by employing amorphous Ge, hcp-Ti/Ge, and hcp-Ru underlayers [2)]. The *c*-axis of CoCr-alloy crystal is well controlled perpendicular to the substrate surface, and the crystal grain diameter distribution is narrowed for the films with hcp-Ti/Ge and Ru underlayers. The distributions of crystal grain diameter for Ti and Ru crystals are relatively narrow when the underlayer materials are deposited on neutral-type amorphous layers. The perpendicular magnetic anisotropy was enhanced greatly by introducing such underlayers.

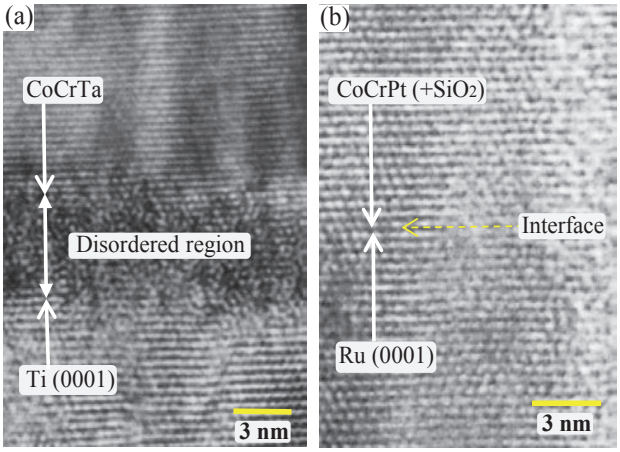

Fig. 2 Cross-sectional high-magnification TEM micrographs showing the interface between recording layer and underlayer [2]. (a) CoCrTa film deposited on Ti (0001) underlayer, (1991) [47]. (b) CoCrPt-SiO_x thin film deposited on Ru (0001) underlayer, (2008).

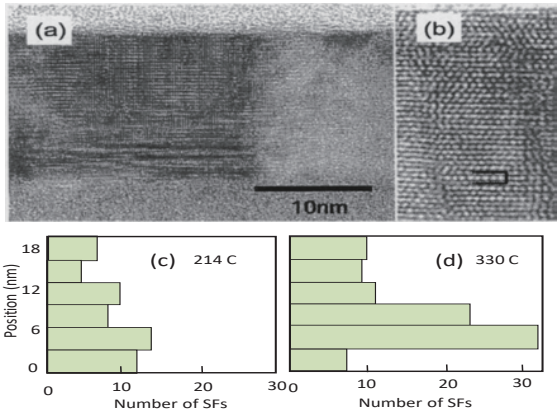

Fig. 3 Distribution of stacking faults (SFs) in CoCrPt recording layer (2002).
(a) Cross-sectional TEM image, (b) high-resolution image showing an example of stacking fault, (c) SF distribution along a CoCrPt layer grown at a substrate temperature of 214 °C, (d) SF distribution along an another CoCrPt layer grown at 330 °C. The structure is CoCrPt(18 nm)/NiTaZr/Glass substrate [52].

With increasing linear recording density, the perpendicular coercivity must be increased while the recording layer thickness needs to be reduced to enhance the writing efficiency of a recording head. In the nearly 30 years since the PMR invention in 1976, the recording layer material varied from a binary CoCr-alloy to ternary or more complex alloys of CoCrTa, CoCrPt, and CoPtCr + X (X = Ta, Si, Nb, B, oxides). The shift was necessary for increasing the K_u value of recording layer, which was directly related with increasing the perpendicular coercivity. When the layer thickness was decreased for Co-alloy recording layer materials to be less than 50 nm, a notable decrease in perpendicular coercivity was observed and the decrease depended on the underlayer material [12, 45, 46]. Careful examinations of the interface between the Co-alloy recording layer and the underlayer revealed that there was an atomically disordered region of a few nanometers around the interface [38, 46, 47]. Figure 2(a) shows the TEM image of initial growth region observed for a CoCr-alloy film deposited on a Ti underlayer [2, 47]. The formation of disordered region was partially due to a large lattice misfit of about 15% between the CoCr-alloy magnetic material and the Ti underlayer, and also due to an inter-diffusion of elements which was caused during a deposition process at an elevated substrate temperature of around 250 °C. An introduction of nonmagnetic layer with hcp-crystal structure such as $CoCr_{35}$, $CoCr_{25}Ru_{25}$, or Ru, which possessed a lattice constant close to that of the Co-alloy recording layer material, was proved effective in forming a sharp elemental interface while keeping an epitaxial relationship between the two layers [12, 46-50]. Compositional variations across the interface were investigated by using a TEM equipped with an EDX, and it was confirmed that the distance of elements diffusion from the underlayer toward the magnetic layer was very small, less than the electron-beam diameter of 2 nm employed in the EDX analysis [49]. An example of CoCrPt (+SiO_2) magnetic layer deposited on a Ru layer is shown in Fig. 2(b). Formation of atomically sharp interface was proved effective in maintaining high perpendicular coercivities of PMR media for reduced magnetic layer thicknesses.

Another origin that deteriorates the perpendicular magnetic anisotropy is stacking faults (SFs) in the hcp-Co-alloy crystal. When a SF exists in an hcp-Co-alloy crystal, the local atomic stacking sequence becomes similar to that of fcc-structure. The magnetic anisotropy of fcc-Co with cubic symmetry is one magnitude lower than that of hcp-Co [51]. Perpendicular coercivity decreases when SFs exist in the crystals of hcp-Co-alloy recording layer. Distribution of SF was investigated for the Co-alloy recording layers using a high-resolution TEM and it was revealed that it depended on the process condition like substrate temperature, deposition rates of recording layer, underlayer, and intermediate layer materials. An example of such analysis on the distributions of SF along CoCrPt crystal columns is shown in Fig. 3 [52]. The recent investigations on CoPt-alloy materials have shown that the atomic attacking sequence is also influenced by the average number of valence electrons of alloy material, and the SF density decreases when the number approaches to a certain value through adjustment of compositional alloy elements [53]. In PMR media productions, the media structure and the process conditions are carefully controlled to lower the SF density in the recording layer.

3. Compositional structure of recording layer

Compositional fluctuations of Co and Cr in vacuum

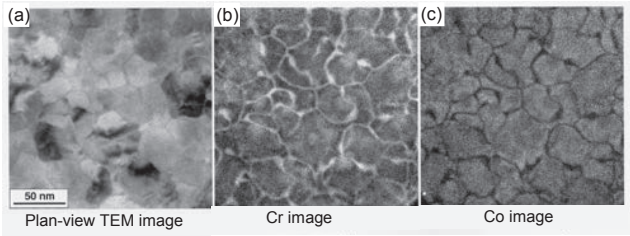

Fig. 4 Cr and Co distributions in a CoCrTa perpendicular medium deposited at 230 °C investigated by EELS-TEM (1996), (a) plan-view TEM image, (b) Cr distribution map, and (c) Co distribution map [66, 67].

evaporated or sputter deposited CoCr alloy thin films were studied initially from a viewpoint to explain the magnetic property differences between thin film and bulk samples, and they were investigated by using NMR [54], FMR [55], chemical etching [56-58], and TEM equipped with an analytical facility in middle to late 1980's [59, 60]. It was in late 1980's when a relation between the non-magnetic Cr concentration in LMR-CoCrTa recording layer and the medium noise property was investigated and it was demonstrated that a Cr-rich CoCrTa thin film medium showed a lower noise property [61-65]. Magnetic crystal grain isolation while controlling the diameter in the recording layer was realized necessary for high-density perpendicular magnetic recording to increase the coercivity, the recording resolution and to decrease the medium noise. Magnetic decoupling and/or reduction of interaction between the neighboring magnetic crystal grains were achieved by enhancing segregation of nonmagnetic metallic elements (Cr, Ta, etc.) toward crystal grain boundaries. The technology has been improved, from around the year 2000, by employing a technique of nonmagnetic material (SiO_x etc.) precipitation along the magnetic crystalline grain boundaries, which is based on a physical segregation of two different phases, metallic magnetic and nonmagnetic amorphous materials, during a film formation process. Figure 4 shows the Cr and the Co distributions visualized for a Co-17at%Cr-3at%Ta PMR medium, where nonmagnetic Cr atoms are strongly segregated near the grain boundaries and are depleted inside the crystal grains [66, 67]. The distribution of Co atom is showing an opposite tendency. When the Cr concentration in a CoCr-alloy material exceeds 30 at. %, the material becomes nonmagnetic at room temperature.

Employment of a sputter deposition system with ultra-high-vacuum background pressure [37, 68] and with a high purity Ar sputtering gas were shown effective in enhancing nonmagnetic elements segregation toward the magnetic crystalline grain boundaries [69]. The residual gasses in a sputter deposition chamber such as water-vapor deteriorate the perpendicular magnetic properties through selective reaction with active Cr atoms forming oxides and/or hindering segregation within the magnetic crystal grains [70]. Strong Cr segregation around the

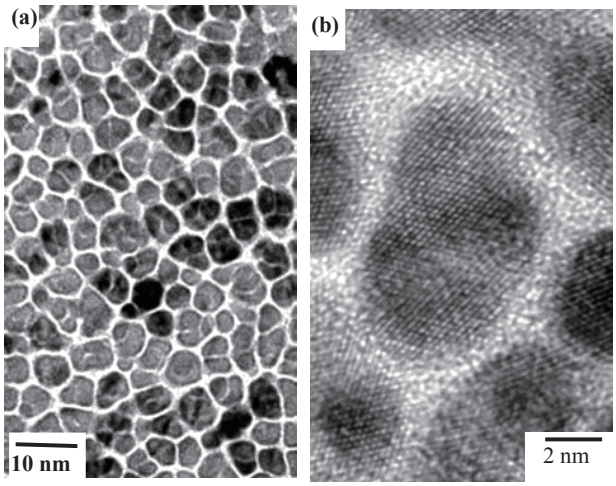

Fig. 5 Plan-view TEM images of CoCrPt-SiO_x perpendicular medium, (2008). (a) TEM image showing the magnetic crystal grains isolated by thin oxide layer and (b) high magnification TEM image [88].

magnetic crystal grains weakens or decouples the direct magnetic exchange between the neighboring magnetic crystal grains, thus contributing to a reduction of medium noise, an increase of coercivity, and an increase of recording resolution.

The high-density magnetic recording demonstration using PMR in the year 2000 [10] was performed by employing CoCr-alloy perpendicular media with enhanced Cr segregation around the magnetic crystal grain boundaries [48, 71]. Although the low noise and the high recording resolution properties were achieved with the media, time dependent decays of recorded signals were observed particularly at low linear densities [72, 73]. This was because that the remanent magnetization M_r was lower than the saturation magnetization M_s, $M_r/M_s<1$, where a demagnetization field was working in an opposite way to the recorded bit direction and caused a time-dependent thermal decay in the recorded information. Although the necessity of media preparation with squareness, $M_r/M_s = 1$, was realized for suppressing such time-dependent thermal decay of signal, the M_r/M_s values of CoCr-alloy media were less than 1 up to the late 1990's [71-73]. Magnetic multilayers composed of Co and noble metals (Co/Pt, Co/Pd) were, on the contrary, known to be tuned easily to possess the value, M_r/M_s, to be 1, and they were investigated as practical magnetic recording media [74, 75-79]. However, the multilayer structure which needed complicated film deposition processes was one of the drawbacks of media production. A novel technology in increasing the M_r/M_s to be nearly unity while achieving a magnetic grain isolation was developed from the year around 2000. The technology introduced oxygen into the Co-alloy thin films, which had a similarity with that of the magnetic tape technology that employed low noise Co-CoO recording layers [80-82].

Addition of oxygen or oxide to a CoPt or a CoCrPt magnetic material during the sputter deposition process

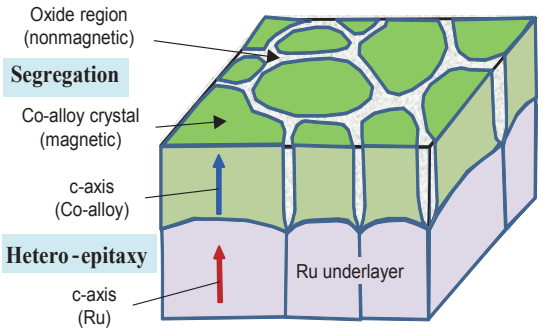

Fig. 6 Structure model of CoCrPt-SiO_x perpendicular medium. Co-alloy magnetic crystals are epitaxially grown on *c*-axis oriented Ru crystals. Thin oxides are separating magnetic interaction between Co-alloy crystal grains[126].

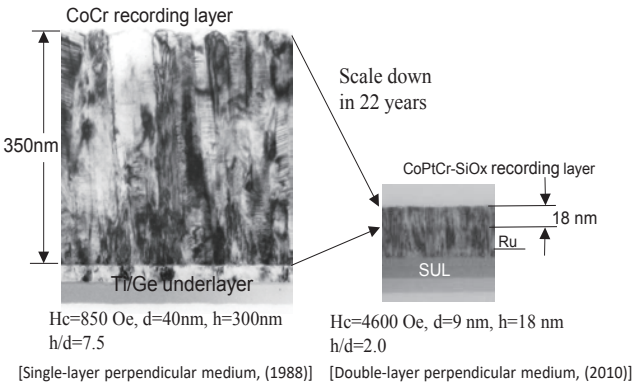

Fig. 7 Comparison of perpendicular recording media. Recording layer height (*h*) and grain diameter (*d*) have been reduced greatly while perpendicular coercivity has been increased in the 22 years from 1988 to 2010 [2].

showed a drastic effect in enhancing the magnetic crystalline grain isolation. The technology was first applied to CoPt media in 1994 [83] and then to CoPtCr media in 2000 [84]. Perpendicular magnetic properties including the coercivity and the squareness (M_r/M_s) were greatly improved by addition of oxides like SiO_x, which were carried out in the early years of this century, accelerated the realization of commercial PMR HDDs [85, 86]. A plan-view TEM image of CoCrPt-SiO_x perpendicular medium is shown in Fig. 5. The compositions of CoCrPt-SiO_x perpendicular media were studied by employing a TEM equipped with an EDX facility, where the local compositions of 1 - 2 nm in diameter area could be determined. With this type media, the magnetic crystal grains of sub-10 nm in diameter are separated by oxide-based grain boundaries of around 1 nm width and this type granular media have been used as the recording media of commercial HDDs. The high magnification TEM image clearly indicates that most of the grains are single crystals and the grain boundary structure is amorphous. The grain boundary compositions were investigated, and it was found that not a small amount of metallic elements other than Si were included in the grain boundaries [87-89]. The metallic elements (Co, Cr, Pt, etc.) are considered to be dissolved in the matrix SiO_x through forming oxides like CoO and Cr_2O_3. The composition indicates that the grain boundary is non-magnetic and the thin oxide layer is drastically reducing the magnetic interaction between the neighboring magnetic crystal grains. A model of PMR medium[126], based on the structural and the compositional investigations, is depicted in Fig. 6. Various nonmagnetic materials such as C [90], SiO_2 [91], TiO_2 [92], Ta_2O_5 [93], etc. have been investigated for magnetic crystal grain isolation of hcp-Co-alloy materials. Although any nonmagnetic material that segregates along the grain boundary during a sputter deposition process is possible for magnetic crystal grain isolation, practical conditions in a mass-production of recording media including easy handling, homogeneity of nanostructure, reproducibility in the fabrication, etc. are considered. As a result, SiO_x-based oxide materials are now widely employed in the commercial PMR media fabrication.

4. Tuning the nanostructure of recording layer

Figure 7 compares the cross-sectional TEM micrographs of Co-alloy PMR media developed in middle 1980's and in 2010 showing the development of nanostructure in over a quarter century. While achieving a drastic scale down in the length and the width of *c*-axis oriented Co-alloy crystal grain, the medium coercivity was increased from around 0.8 kOe to be larger than 4 kOe by controlling the alloy composition, the underlayer material, and the processing condition, all of which were inevitable in increasing the areal density. The PMR media used in commercial HDDs employ the double magnetic layer structure consisting of a semi-hard magnetic recording layer stacked on a soft magnetic underlayer, which is the basic PMR structure proposed by Prof. Iwasaki [1]. Until late 1990's, the Co-alloy recording layer was deposited directly on a thick soft-magnetic underlayer of crystalline Fe-Ni [94, 95], amorphous Co-Zr-Nb [11, 96], etc. However, a series of research has shown that the medium noise can be reduced by introducing a thin nonmagnetic layer between the soft magnetic underlayer and the semi-hard recording layer, where the nonmagnetic layer is now defined as an intermediate layer since the soft magnetic layer is called as "underlayer" in the double layer structure [97]. Such magnetic decoupling between the two magnetic layers was effective in preventing a transmission of short wave length noise caused in the soft magnetic underlayer [98-100].

The introduction of nonmagnetic interlayer offered another positive effect in controlling the structure of recording layer independently from that of soft magnetic

underlayer (SUL), where a smaller thickness SUL was desirable in achieving an efficient magnetic writing with a single-pole writing head. As explained in the previous section, the nanostructure of recording layer must be controlled simultaneously in the crystal orientation, the grain diameter, as well as the separation between magnetic grains with a presence of thin nonmagnetic layer. Dual layer structures of hcp-Ru/Ta [42, 43], hcp-Ru/Ni-W, or even more complicated stacked structures [101, 102] were employed as the intermediate layer, where the first layer of Ta or Ni-W provided a surface condition that promoted free nucleation of hcp-Ru crystal with the (0001) basal plane, energetically most stable plane, parallel to the surface. A sputter deposition consisting of low Ar pressure deposition followed by high Ar pressure deposition for the Ru layer preparation was employed to produce an intermediate layer with the *c*-axis oriented dome-like Ru crystal grains which were effective in enhancing nonmagnetic SiO_x segregation around the Co-alloy magnetic crystal grains [101, 102]. The Ar pressure for sputtering is known to give an influence on the topological nanostructure of deposited film [103].

Since a PMR medium is used in combination with a magnetic head in an HDD system, a careful adjustment in the magnetic property of recording layer is carried out through an optimization not only from the intermediate layer but also for the Co-alloy composition, the nonmagnetic material for magnetic crystal separation, the sputter deposition condition, etc. Magnetic property control along the thickness of Co-alloy recording layer by employing a compositional gradient technique or a deposition of layers with different properties was used for tuning the medium property suitable for high areal density PMR [101, 104, 105].

5. Recorded magnetization structure

Magnetization structure observation gives valuable information for the investigations on the inter-relationship between medium structure and recording characteristics of recording resolution and medium noise. Bitter method is the easiest technique and it was applied in middle 1980's to investigate the effect of *c*-axis orientation of CoCr-crystal grains on perpendicular magnetization. An example is shown in Fig. 8. The Bitter observation from the top and the bottom sides of recording medium showed that a stronger perpendicular magnetization was realized for a medium with higher *c*-axis orientation [106]. More quantitative estimation of perpendicular magnetization was later carried out in 1986 - 1987 by using the electron holography technique[106-108]. Figure 9 shows the electron holography images of CoCr-alloy media with different degrees of *c*-axis orientation observed for the media cross-sections. The data showed that a perpendicular magnetization at 300 kFCI (bit length = 80 nm) recording was achieved through the whole film thickness of 200 nm for the highly *c*-axis oriented CoCr medium sample, indicating that the

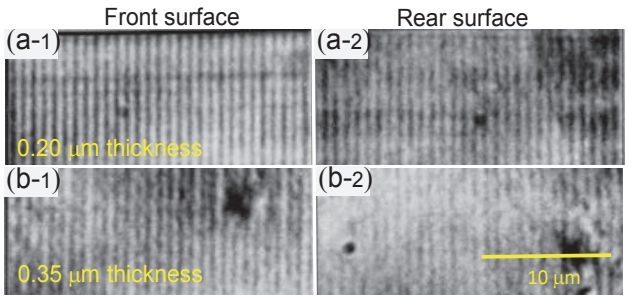

Fig. 8 Optical microscope images of recorded magnetization observed by Bitter method. CoCr perpendicular thin film media with thicknesses of 0.20 and 0.35 μm were observed from the front and the rear surfaces, (1987).
Bitter images of 20 kFCI recording on a 0.20 μm thick CoCr/Ge perpendicular thin film observed from (a-1) top and (a-2) rear surfaces.
Bitter images of 20 kFCI recording on a 0.35 μm thick CoCr/Ge perpendicular thin film observed from (b-1) top and (b-2) rear surfaces [106].

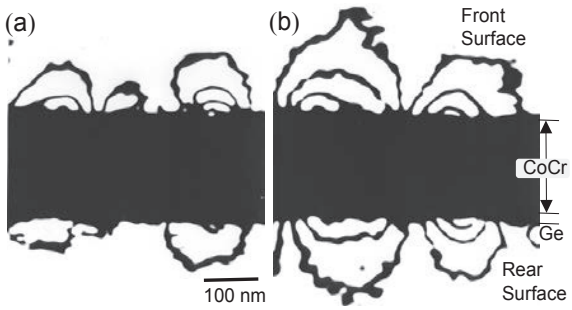

Fig. 9 Electron holography images of magnetization recorded at 300 kFCI observed for cross-sectional CoCr perpendicular media samples without and with Ge underlayer, (1987).
Magnetic leakage flux intensity is different between the front and the rear surfaces for a CoCr film without underlayer (a).
Magnetic leakage flux intensity is similar at the front and the rear surfaces, indicating a strong perpendicular magnetization is realized for the film with Ge underlayer (b) [106-108].

medium structure, particularly the alignment of easy magnetization orientation, was giving a very strong influence in achieving a high linear density magnetic recording.

Magnetization structure observations were also carried out by employing high-resolution magnetization observation techniques such as Lorentz TEM [109], spin SEM [110], and magnetic force microscopy (MFM) [37, 75, 111-113]. MFM is the technique developed as an extension of scanning force microscopy invented in 1986 [114] and the technique started to be employed in the magnetics community from late 1980's. Since then, MFM has been most widely used to visualize the recorded information because of its easy operation and no special requirement of pre-processing for the observation samples. Figures 10 (a) and (b) compare the magnetization structure of PMR- and LMR-CoCrTa media with similar alloy

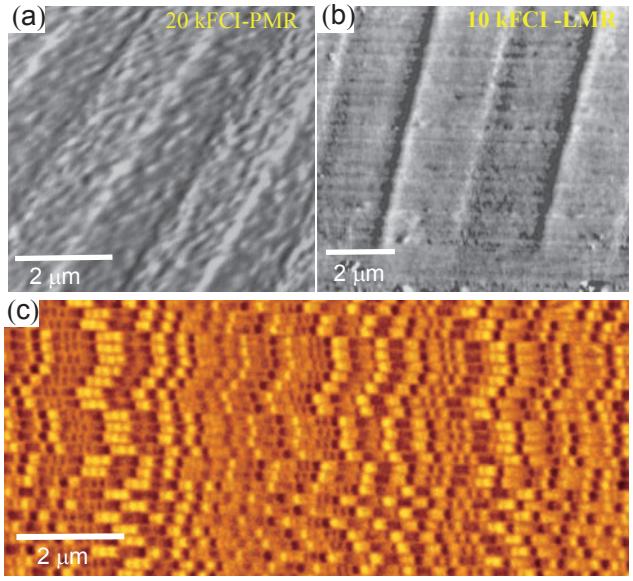

Fig. 10 MFM images of magnetization structure recorded on Co-alloy recording media, (a), (b): (1994, and (c) (2007) [2,113]. (a) MFM image of Co-17at%Cr-5at%Ta perpendicular medium recorded at 20 kFCI. (b) MFM image of Co16at%Cr-4at%Ta longitudinal medium recorded at 10 kFCI. (c) MFM image of commercial PMR medium shipped in 2007 with an areal density of 185 Gb/in^2.

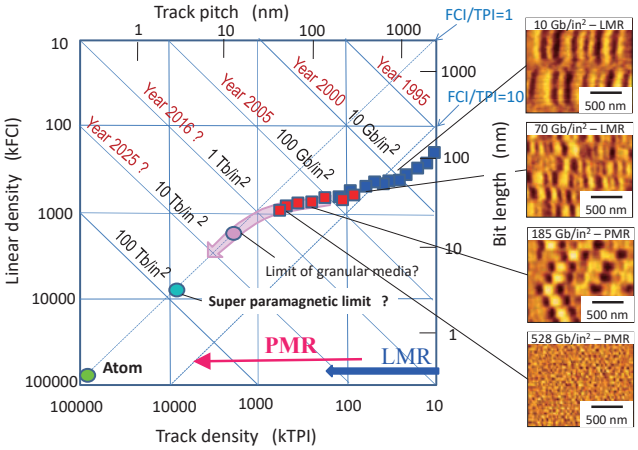

Fig. 11 Decreasing trend of bit size in commercial HDDs [2].

compositions observed in 1994 [113]. The LMR medium was observed with a relatively uniform MFM contrast within sharply recorded bit transitions, whereas the PMR medium was with an irregular MFM contrast and wavy bit transitions which correspond to higher medium noise and poorer recording resolution. The difference in magnetization structure was correlated with the nonmagnetic elements (Cr, Ta) segregation around the magnetic crystal grain boundaries, which was later confirmed to be depending on the crystal grain boundary structure. When deposited under a similar condition, enhanced segregation was achieved more easily with an LMR medium that included higher-angle crystal grain boundaries, whereas segregation of nonmagnetic elements was poor for a PMR medium consisting of *c*-axis oriented hcp-crystal grains which tended to form lower-angle crystal grain boundaries. The crystal lattice of *c*-axis oriented hcp-grain in PMR medium matches with that of neighboring crystal every 60 degrees of rotation along the perpendicular direction, whereas that of LMR medium with the *c*-axis lying in the film plane matches every 180 degrees and therefore crystal grains of LMR medium tend to form large angle crystal grain boundaries. Because the local stress in crystal grains of LMR medium presumably larger than that of PMR medium, Cr segregation was accelerated for the LMR medium.

The amorphous phase segregation along magnetic crystalline grain boundaries by employing SiO_x oxide as the nonmagnetic material sputter deposited together with a CoPt-alloy magnetic material, which was based on a two-phase separation mechanism, showed a drastic effect in forming very sharp compositional transitions from magnetic to nonmagnetic regions. As a result, smaller-size recorded bits surrounded by sharp magnetization transitions became possible as shown in the MFM image of CoCrPt-SiO_x perpendicular media depicted in Fig. 10 (c). The signal to noise ratio was improved and thus the continuous decrease in bit size became possible while keeping the thermal stability of recorded information which had caused problems with LMR media [7, 8]. The decreasing trend of bit size in commercial HDDs is shown in Fig. 11 together with related MFM images [2]. The bit shape is changing from an elongated rectangular to a square with increasing areal density and by shifting the recording technology from LMR to PMR.

With increasing areal density toward 1 Tb/in^2, the bit length is decreasing to be shorter than 25 - 30 nm where a spatial resolution of 10 nm or better is necessary to clearly observe the recorded bit patterns. Since the spatial resolution of commercially available MFM tip was limited at around 20 nm, the structure and the magnetic material for MFM tip fabrication were systematically investigated to improve the spatial resolution and the magnetic switching field [115-119]. High magnetic switching field is required for an MFM tip in the magnetization structure observation of high coercivity medium, where the tip is exposed to a strong magnetic flux emanating from the sample that may change the tip magnetization. When the tip magnetization changes, the MFM contrast varies during an observation process. MFM tips with high magnetic switching fields were prepared by coating high K_u magnetic materials on nonmagnetic base tips [120-122]. Through optimization of tip fabrication condition, MFM tips with spatial resolutions of 6 - 7 nm could be developed [123, 124]. The switching field was increased to be higher than 2 kOe with maintaining high spatial resolutions of 10 nm or better [117, 125].

Figure 12 shows the magnetization structure of 500 -

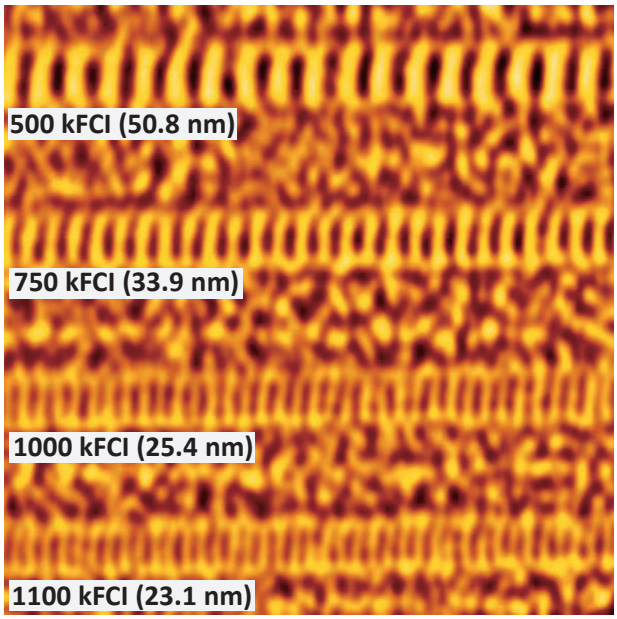

Fig. 12 Magnetization structure of 500 – 1100 kFCI (bit length: 50.8 – 23.1 nm) recording on a CoCrPt-SiO_x PMR medium observed by using a high-resolution MFM tip, (2013) [118, 119].

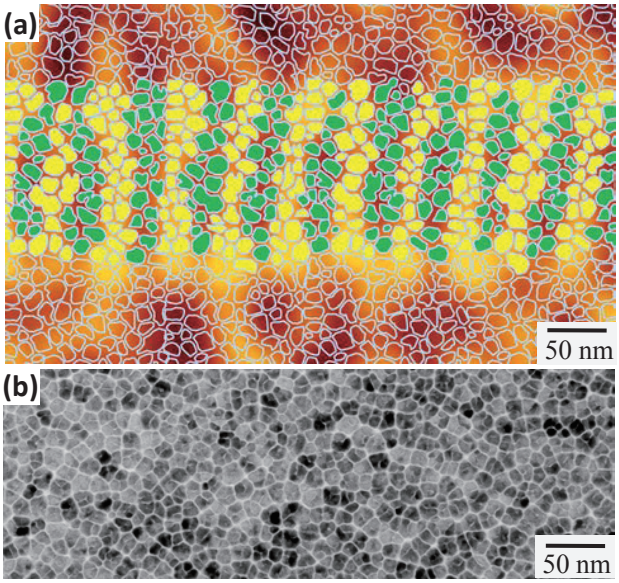

Fig. 13 Relationship between magnetization structure (1000 kFCI recording) and magnetic crystal grain distribution, (2013). The schematic MFM image, (a), is obtained by overlapping an MFM image with a plan-view TEM image, (b), observed for a same PMR medium [118,119].

1100 kFCI (bit length: 51 - 23 nm) recorded on a CoCrPt-SiO_x PMR medium observed by employing a high-resolution tip [119]. When a plan-view medium structure observed by TEM is overlapped with an MFM image, a relationship between the recorded magnetization and the magnetic crystal grain structures can be demonstrated as shown in Fig. 13 [118]. Here, the magnetic crystal grains along one track are colored for easy recognition of the inter-relationship. Although the two pictures (MFM and TEM images) were not observed for a same area but from different areas of a same medium sample, a detailed information how the individual bit is recorded on granular magnetic crystal grains can be revealed, which is useful in finding the points for further improving the medium structure to be more suitable for higher areal density magnetic recording [126].

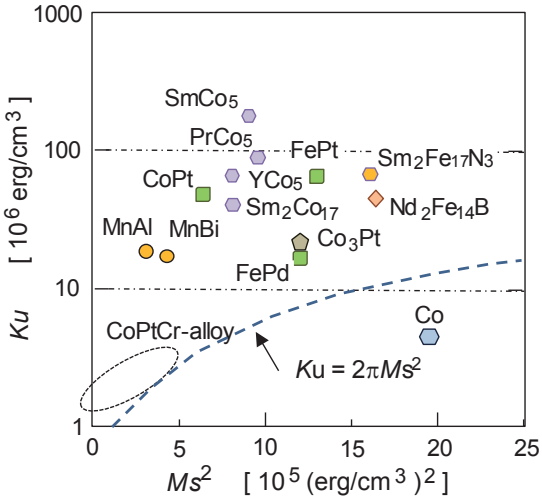

Fig. 14 K_u values of magnetic materials plotted as a function of M_s^2 [127-129].

6. Nanostructure tailoring of magnetic materials

6.1 High K_u magnetic materials

The K_u value of CoCrPt-alloy material used as the recording layer in the current HDDs is limited to be around 10^7 erg/cm^3 even the alloy composition and the media production process conditions are modified. Magnetic materials with higher K_u values are required for further increasing the recording density. The volume (V) of magnetic crystal grain included in a magnetic bit of recording layer needs to be continuously decreased while keeping the thermal stability condition of recorded information, $K_u V/k_B T$ > 35-70 [127, 128], where k_B is Boltzmann's constant and T is absolute temperature. There are candidates for such magnetic materials with K_u values greater than 10^7 erg/cm^3; (1) magnetic multilayers of Co and noble metals, Co/Pd, Co/Pt, (2) ordered alloys of rare-earth and 3d-transition metals, $SmCo_5$, $PrCo_5$, $GdCo_5$, Sm_2Co_{17}, etc., (3) alloys of 3d-transition and noble metals with ordered structures, $L1_0$-FePt, $L1_0$-FePd, $L1_0$-CoPt, $D0_3$-Co_3Pt, τ-MnAl, (4) Co-Pt alloys with metastable ordered structures, $L1_1$-CoPt, B_h-CoPt, and (5) other compounds, $Nd_2Fe_{14}B$, $Sm_2Fe_{17}N_3$, α-MnBi, etc. Figure 14 shows the K_u values of magnetic materials plotted as a function of Ms^2, which are cited from the references[127-129]. For application to PMR media, the K_u should be larger than the magneto-static energy ($2\pi M_s^2$), thus a relation, $K_u > 2\pi M_s^2$, must be satisfied. The materials above the $K_u = 2\pi M_s^2$ line shown in Fig.

14 are basically applicable to PMR media. However, for practical applications, several conditions such as for aligning the easy magnetization axis perpendicular to the substrate, for achieving higher order degrees in ordered alloys to get high K_u values, for controlling the crystal grain size suitable for magnetic recording, chemical stability, etc. must be considered. These conditions are usually different depending on the material and thus must be investigated independently for the respective magnetic material. Some of the basic conditions in tailoring the crystal structure, the crystal orientation, the chemical ordering, etc., have been investigated by employing epitaxial magnetic thin films prepared on nonmagnetic single-crystal substrates. For example, it has been shown that the easy magnetization axis of $SmCo_5$ ordered alloy and related compounds of RT_5-type ordered structure (R: rare-earth element, T: 3d-transition element), YCo_5, $GdCo_5$, $SmNi_5$, $SmFe_5$, etc., which possess K_u values in the order $10^6 - 10^8$ erg/cm^3, can be aligned perpendicular to the substrate by employing a Cu(111) [130-137] or a Ru(0001) underlayer [138]. The effects of deposition temperature and film composition on the formation of ordered alloys and the degree of ordering are also investigated by using an UHV-MBE with co-evaporation of R and T elemental materials. Amorphous phases tend to be mixed with RT_5-ordered crystals when the composition shifts from the optimum ranges which depend delicately on the R-T material combination [130, 134]. Substrate temperature higher than 500 °C is necessary for the preparation of RT_5-type epitaxial thin films on Cu(111) and Ru(0001) underlayers. Higher temperature, however, promotes diffusion of metallic Cu or Ru to the magnetic layer [131, 139], which generally lowers the K_u value. Further studies for forming a sharp interface while achieving a high order degree in the RT_5 structure in very thin films of less than 10 nm in thickness are apparently necessary for the application to future perpendicular recording media. Chemical stability of RT_5 material is an issue to be solved before practical applications, since rare-earth elements react easily with oxygen or water vapor.

6.2 Magnetic multilayer films

Magnetic multilayers of Co and noble-metal element (Pd or Pt) can be prepared at relatively low temperatures. From the investigations of Co/Pd multilayers deposited on single-crystal Pd underlayers of (001), (011), and (111) orientations at RT, it was shown that higher perpendicular magnetic anisotropies were observed for the epitaxial multilayer films prepared on fcc-Pd(111) underlayer [140, 141]. The multilayer was composed of repeated number of stacked fcc-Co(111)/fcc-Pd(111) bi-layer with very thin Co-Pd alloyed regions at the Co/Pd interface [142-144]. Perpendicular magnetic anisotropy increased with increasing the repetition number, and the origin was interpreted to be coming from an interface anisotropy and a magneto-crystalline anisotropy of Co-Pd(111) alloy-crystal whose lattice was slightly deformed along the perpendicular direction in accommodation of a large lattice misfit of 9.2% between the fcc-Co and the fcc-Pd layers [145]. As no ordered phase exists in the Co-Pd binary phase diagram [146], the origin of perpendicular anisotropy is possibly due to a presence of very thin metastable structure similar to $L1_1$-phase which has a high K_u and is recognized in a CoPt alloy material [147].

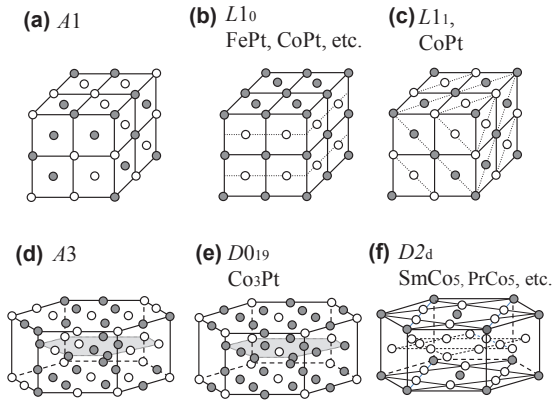

Fig. 15 Crystal structures of high K_u magnetic materials, based on fcc-cubic ($A1$) and hexagonal ($A3$) lattices.

The magnetic anisotropy and the saturation magnetization can be controlled in a certain range to be usable for magnetic recording media by varying the thickness ratio of the Co and Pd layers and the repetition number of Co/Pt bi-layer. Although a low substrate temperature for film formation and a high perpendicular magnetic anisotropy are the advantages with multilayer magnetic films, they are not easy to be tuned for application to granular-type perpendicular media. The multilayer films are considered to be more suitable for the bit patterned media which involve nanometer scale fabrications using chemical etching, ion-beam, or other sophisticated techniques [148-150].

6.3 Magnetic materials with ordered structures

The high K_u magnetic materials of (2) - (5) groups are with ordered structures consisting of more than two elements with atomic arrangements specific to the respective ordered structures. Figure 15 shows the typical crystal structures of high K_u magnetic materials. Table 2 lists the structural and magnetic properties of high K_u magnetic materials [127-129, 151-156]. The degree of atomic ordering in a magnetic material, where a higher order degree corresponds to a higher K_u value, depends on the processing condition, in particular, the temperature. Thus higher substrate temperatures are generally necessary for film preparations. In these high K_u magnetic materials, the alloys of 3d-transition and noble metals with $L1_0$-type ordered structure, $L1_0$-FePt, $L1_0$-FePd, and $L1_0$-CoPt alloys, have been most intensively investigated for the granular-type recording layers [127, 128, 157-161]. Thus, high K_u magnetic materials with $L1_0$ ordered structure are focused in the present

Table 2 Structure and magnetic properties of high K_u magnetic materials [127-129, 151-156].

Material	Crystal structure	K_1, (10^7 erg/cm^3)	M_s, (emu/cm^3)	T_c, (K)
$L1_0$ phases	Tetragonal (*fcc*-based)			
FePt	a = 384 pm, c = 370 pm, c/a = 0.96	6.6	1140	750
FePd	a = 381 pm, c = 372 pm, c/a = 0.98	1.8	1100	749
CoPt	a = 377 pm, c = 370 pm, c/a = 0.98	4.9	770	840
τ-MnAl	a = 392 pm, c = 357 pm, c/a = 0.91	1.7	560	650
$B8_1$ phase	Hexagonal			
α-MnBi	a = 428 pm, c = 611 pm, c/a = 1.43	1.2	700	633
$L1_1$ phase	CuPt-type rhombohedral (*fcc*-based)			
CoPt	a = 534 pm, α = 61.5°	3.7 (S = 0.54)	800	-
$D0_{19}$ phase	Rhombohedral (*hcp*-based)			
Co_3Pt	a = 367 pm	2.0	1100	1190
Compounds of rare-earth and transition elements	Hexagonal			
$SmCo_5$	a = 499 pm, c = 398 pm, c/a = 0.80	11 - 20	910	1020
YCo_5	a = 494 pm, c = 398 pm, c/a = 0.81	5 - 6.5	850	987
$PrCo_5$	a = 501 pm, c = 399 pm, c/a = 0.80	8.3	930	885
$GdCo_5$	a = 498 pm, c = 397 pm, c/a = 0.80	4.6	498	1014
Sm_2Co_{17}	a = 838 pm, c = 1221 pm, c/a = 1.45	4.2	838	1190
$Sm_2Fe_{17}N_3$	a = 873 pm, c = 1264 pm, c/a = 1.45	8.6	1230	749
	Tetragonal			
$Nd_2Fe_{14}B$	a = 879 pm, c = 1218 pm, c/a = 1.39	4.6	1270	588

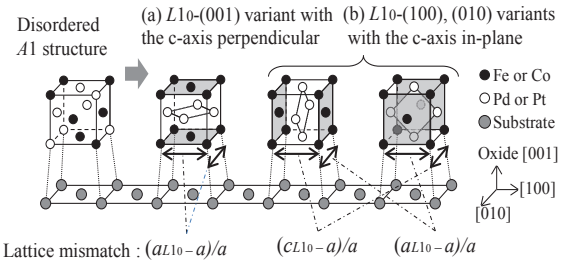

Fig. 16 Possibilities of phase transformation from disordered $A1$ structure to $L1_0$ ordered structure. The c-axis of $L1_0$(001) variant crystal is perpendicular to the substrate surface, whereas the c-axis is in-plane for the $L1_0$(100) and (010) variant crystals. The lattice mismatch is supposed to give an influence which type of variant crystal is likely favored.

review. Concerning the preparation and the characterization of other-type ordered alloy films of RT_5, $L1_1$-CoPt, B_h-CoPt, and DO_{19}-Co_3Pt, they are reported in the references [130-139, 162-172].

There are technical issues associated with the materials of $L1_0$ ordered structure to be solved for application to PMR recording media. They are basically similar to the case of conventional Co-alloy material with an hcp structure, but are more complicated. The technologies for aligning the easy magnetization axis of $L1_0$-magnetic-crystal grain perpendicular to the substrate surface and for preparation of a flat medium surface that can allow a very narrow spacing of less than a few-nm between the medium and a magnetic head. The latter is a newly added issue associated with the magnetic material which will be used for HDDs with the areal densities greater than 2 - 3 Tb/in^2, where a new-type media, bit patterned media (BPM), is included. Preparation of magnetic crystal with $L1_0$-ordered structure involves atomic ordering from a disordered fcc ($A1$ structure), which is different from the case of traditional Co-alloys. The possibilities of easy magnetization distribution associated with the phase transformation from $A1$ to $L1_0$ ordered structure are shown schematically in Fig. 16. Here, the underlayer of oxide with NaCl-type structure is assumed, considering that magnesium oxide (MgO: NaCl-type structure) has been widely used as an underlayer for aligning the easy magnetization axis (c-axis) perpendicular to the film plane. $A1$ structure based crystallographic notations for the direction and the plane are employed in this paper for the $L1_0$-ordered structure to make easy comparison with those of $A1$ structure, though the unit-cell of $L1_0$-ordered structure is tetragonal as shown in Table 2.

The easy magnetization axis of $L1_0$-orederd magnetic crystal is the c-axis. When an atomic ordering takes place in a bulk crystal of $A1$ structure, there are three possibilities of c-axis orientation with the ordered $L1_0$ structure, $L1_0$ [100], [010], and [001] parallel with respect to the original $A1$ [001], as shown in Fig. 16. Three kinds of $L1_0$ crystal domain variant with the c-axis perpendicular each other were observed in the high-resolution TEM pictures of FePt film samples prepared on NaCl(001) substrates [173, 174]. The presence of crystal domains with the c-axis lying in the film plane deteriorates the perpendicular magnetic anisotropy and widens the magnetic switching field distribution of media, both of which are undesirable for high density magnetic recording applications.

The other issue is the surface roughness of granular-type magnetic layer consisting of $L1_0$ ordered magnetic crystal grains. Possibly due to a large difference in surface energy between the magnetic material (FePt, FePd, or CoPt) and the oxide underlayers (MgO, etc) and to a high substrate temperature for enhancing $L1_0$ ordering, the magnetic material tends to form crystal grains of spherical or facetted shape with different diameters forming notable surface undulations, which may hinder a closer approach of magnetic head in performing a high density magnetic recording. Basic technologies in controlling the crystallographic orientation and in forming thin films with reduced surface undulations are briefly explained in the following sections.

(a) *c*-axis alignment of $L1_0$-ordered magnetic crystal

In order to apply $L1_0$-oredered alloy magnetic films to PMR media, the *c*-axis of crystal grain must be aligned perpendicular to the film surface. The alignment involves a more complicated technology compared with the case used for the conventional hcp-Co-alloy crystal. This is because that $L1_0$-crystal structure is based on cubic ($A1$, fcc) structure with three crystallographic symmetries compared with less crystallographic symmetries in the hcp-structure ($A3$). When a magnetic material is deposited on a substrate where an $L1_0$-ordered alloy crystal with the basal $L1_0$-(001) plane parallel to the surface is expected through an epitaxial growth mechanism, there are other possibilities of crystal growth with the $L1_0$-(100) and the $L1_0$-(010) planes parallel to the surface as well. This is due to that the atomic arrangement of $L1_0$-(001) is similar to that of other planes and the unit size of $L1_0$-(001) basal plane ($a \times a$) is very similar to that of other $L1_0$-(100) and $L1_0$-(010) planes ($a \times c$), where the c/a ratios of $L1_0$ crystals are very close to unity ranging between 0.96 and 0.98 for the ordered FePd, FePt, and CoPt materials as listed in Table 2. When the order degree decreases, the c/a ratio approaches to 1.0 [175] thus reducing the difference in lattice dimension between the $L1_0$-(001) basal plane and the other $L1_0$-(010), $L1_0$-(100) planes. As a result, three possibilities of ordering from disordered $A1$ structure to $L1_0$-ordered structure exist as shown schematically in Fig. 16.

Table 3 shows the distributions of $L1_0$-crystal variants which were investigated for FePd, FePt, and CoPt magnetic materials [153, 176]. 40 nm thick films were deposited on the single-crystal substrates of MgO, $SrTiO_3$, and $LaAlO_3$ with (001) orientation at a substrate temperature of 600 °C. The lattice constants of substrate material and the misfits with the magnetic materials are also shown in Table 3. All the magnetic films grew epitaxially on the (001) single-crystal substrates. The $L1_0$-variant configurations and order degrees were carefully investigated by reflection high-energy reflection diffraction (RHEED) and by X-ray diffraction (XRD) employing out-of-plane and in-plane measurements. Similar results on the variant configurations and the order degrees are confirmed for the magnetic materials of 40 nm thickness prepared by employing a two-step process which consists of low temperature deposition at 200 °C followed by high temperature annealing at 600 °C [153, 177]. When the magnetic materials were deposited at 200 °C, the films grew epitaxially with the disordered $A1$ structure. In the case of two-step process, an ordering from disordered $A1$ structure to $L1_0$-ordered structure is taking place during the annealing process at 600 °C. On the $LaAlO_3$(001) substrate, two-types of variant crystal were coexisting for the three magnetic materials. On the contrary, FePd film grew with the $L1_0$-(001) plane parallel to the substrate surface on the MgO(001) and the $SrTiO_3$(001) substrates and the $L1_0$-(100), (010) variants were not recognized. However, two variant crystals were coexisting on the $LaAlO_3$(001) substrate. FePt and CoPt films were consisting of two-types of variant crystal on these oxide substrates. The data indicate that $L1_0$-crystal variant structure changes depending on the combination of magnetic and substrate materials. It also shows that the order degree, S, is different between the $L1_0$-variant crystals with the *c*-axis perpendicular and in-plane for a magnetic film. Higher order degrees tend to be observed for the $L1_0$-(001) variants than for the $L1_0$-(100) + (010) variants as shown in the cases of CoPt on MgO, $SrTiO_3$, and $LaAlO_3$ substrates, FePt on $SrTiO_3$ and $LaAlO_3$ substrates, and FePd on $LaAlO_3$ substrate. Such difference seems to be caused by a delicate difference of atomic movement within a magnetic crystal during the ordering process, which is possibly related with the internal stress of magnetic crystal caused by a lattice misfit with the substrate lattice.

Higher S value of $L1_0$-(001) variant is observed in the order FePd > FePt > CoPt on the oxide substrates, indicating that the activation energy for $L1_0$-ordering is the lowest for the FePd material. When the order degree is compared for the FePd films deposited on MgO, $SrTiO_3$, and $LaAlO_3$ substrates, higher S value is observed in the order MgO > $SrTiO_3$ > $LaAlO_3$. This tendency is similar to the order of lattice misfit, $(a_{L10} - a)/a$, where a_{L10} is the lattice length of $L1_0$-(001) basal plane and a is the lattice constant of oxide crystal. A negative larger lattice misfit along $L1_0$ [100], [010] can be interpreted to yield a higher S value in the $L1_0$-(001) variant. The rule is also applicable for the S value of $L1_0$-(001) variant in CoPt film. The data for FePt film show almost similar tendency but with a reversed order between the $LaAlO_3$ substrate (S = 0.30, misfit = - 0.8%) and the $SrTiO_3$ substrate (S = 0.34, misfit = - 0.2%). The discrepancy may be within an experimental error since the misfit difference is only 0.6%. The stress in $L1_0$-(001) variant crystal caused by a lattice misfit with the substrate is considered to have given a positive effect in enhancing ordering.

Table 3 shows that the ratio of $L1_0$-variants with the *c*-axis perpendicular and in-plane differs depending on

Table 3 $L1_0$ crystal variants in magnetic thin films deposited on different oxide substrates[153, 176].

Substrate	Property	Magnetic material		
		FePd a_{L1_0} = 381 pm, c_{L1_0} = 372 pm	FePt a_{L1_0} = 384 pm, c_{L1_0} = 370 pm	CoPt a_{L1_0} = 377 pm, c_{L1_0} = 370 pm
MgO (001) a = 421 pm	V_{L1_0} (001) S_{L1_0} (001) $(a_{L1_0} - a)/a$	100 % 0.69 - 9.7 %	35 % 0.34 - 8.7 %	41 % 0.23 - 10.0 %
	V_{L1_0} (100), (010) S_{L1_0} (100), (010) $(c_{L1_0} - a)/a$	0 % - -11.8 %	65 % 0.39 -12.1 %	59 % 0.03 -12.1 %
$SrTiO_3$ (001) a = 390 pm	V_{L1_0} (001) S_{L1_0} (001) $(a_{L1_0} - a)/a$	100 % 0.61 - 2.6 %	40 % 0.38 - 1.6 %	48 % 0.20 - 3.3 %
	V_{L1_0} (100), (010) S_{L1_0} (100), (010) $(c_{L1_0} - a)/a$	0 % - - 4.9 %	60 % 0.33 - 5.2 %	52 % 0.06 - 5.1 %
$LaAlO_3$ (001) a = 381 pm	V_{L1_0} (001) S_{L1_0} (001) $(a_{L1_0} - a)/a$	42 % 0.51 - 0.2 %	42 % 0.30 + 0.8 %	40 % 0.15 - 1.0 %
	V_{L1_0} (100), (010) S_{L1_0} (100), (010) $(c_{L1_0} - a)/a$	58 % 0.19 - 2.5 %	58 % 0.22 - 2.9 %	60 % 0.11 - 2.9 %

V_{L1_0} (001): volume ratio of variant with c-axis perpendicular to the substrate. S_{L1_0} (001): order degree of $L1_0$ (001) variants.
$(a_{L1_0} - a)/a$: lattice mismatch between $L1_0$-crystal and the substrate.
V_{L1_0} (100) + (010) : volume ratio of variants with c-axes in-plane. S_{L1_0} (100) + (010) : order degree of $L1_0$ (100) + (010) variants.
$(c_{L1_0} - a)/a$: lattice mismatch between $L1_0$ (100) or (010) crystal and the substrate.

the combination of magnetic material and substrate. Considering the volume ratio (33%) of $L1_0$-(001) variant expected when the phase transformation from $A1$ to $L1_0$ structure is taking place randomly, the nucleation of $L1_0$-(001) variant is apparently favored since the volume ratio exceeds 33% for all the combinations. However, it is not easy to discern which factor is playing a dominant role in fixing the variant orientation. Only the $L1_0$-(001) variant is observed for the FePd films formed on MgO and $SrTiO_3$ substrates, but on $LaAlO_3$ substrate two kinds of variant are coexisting. For FePd film, a larger negative lattice misfit with the substrate seems to be working to promote the nucleation of $L1_0$-(001) variant. However, this rule is not straightforwardly applicable to the FePt and the CoPt cases. Some other material factors such as activation energy of atomic diffusion in magnetic crystal, $L1_0$ crystal nucleation density, and mechanical property like Young's modulus are considered to be working in addition to the lattice misfit effect.

The variant configurations were investigated for the 40 nm-thick $Fe_{50}(Pt_{1-x}Pd_x)$ alloy films deposited on MgO(001) substrate to study the influence of Pd to Pt ratio on $L1_0$ variant structure[178, 179]. The result showed that the films with $x > 0.5$ consisted of $L1_0$(001) crystals, whereas the films with $x < 0.25$ included $L1_0$(100) crystals with the c-axis lying in the film plane. Such data is apparently indicating that material related factors are giving influences in fixing the $L1_0$-variant crystal orientation. The effect of strain caused by lattice misfit on $L1_0$ variant configuration can be investigated by employing film samples with different thicknesses, since the tension force caused by a misfit between the substrate and the deposited magnetic material decreases with increasing the magnetic layer thickness along the film growth direction. The effects of magnetic layer thickness on the variant structure and the order degree were investigated for FePd films deposited on MgO(001) substrates[180]. Although the films thinner than 40 nm consisted of $L1_0$(001) crystal, a notable volume of $L1_0$(100) and $L1_0$(010) variants started to be included when the film thickness was increased to be larger than 100 nm. The easy magnetization axis varied from perpendicular to in-plane, as the thickness was increased from 100 to 500 nm where the volume percentage of $L1_0$(001) variant decreased down to about 20% which is lower than that expected for random nucleation (33%). The order degree of $L1_0$ structure also decreased with increasing the magnetic layer thickness. Similar data were obtained for FePt thin films[181]. These results show that the lattice strain caused by misfit with the substrate material is playing an important role in fixing the $L1_0$ variant configuration and in enhancing the ordering degree.

The effects of variant configuration and the order degree are also investigated for magnetic materials formed on fcc (001) metallic underlayers such as Ag, Au, Pt, Pd metals epitaxially grown on MgO(001) substrates[182]. Although 10 nm thick FePt films deposited at a substrate temperature of 600 °C grew with the c-axis of $L1_0$ structure perpendicular to the substrate surface they included $L1_0$(100) variants. The order degree varied widely in a range between 0.2 – 0.78 depending on the fcc underlayer material, which is different from the cases of oxide substrate. The difference may be attributed to the difference of lattice strain in the magnetic material around the interface between the metallic underlayer and the oxide substrate. In the cases of metallic underlayer, the strain will be more easily relaxed due to similar Young's modulus and possibly due to element's

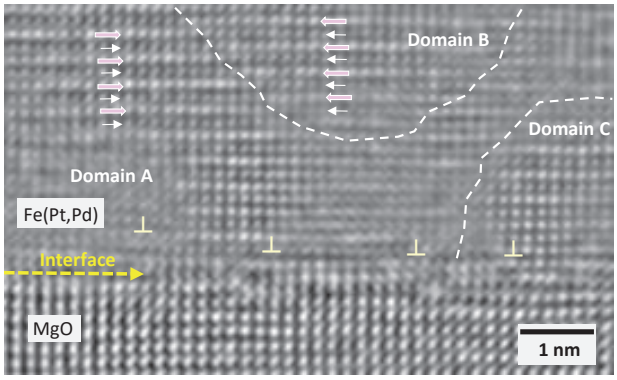

Fig. 17 High-resolution TEM image of interface between MgO(001) substrate and $L1_0$-ordered Fe(Pt, Pd) epitaxial thin film. The thick and thin arrows respectively show the lines enriched with high atomic number atoms (Pt, Pd) and with low atomic number atoms (Fe) corresponding to the atomic stacking along [001] of $L1_0$-ordered structure. The dotted lines show the anti-phase boundaries and the mark ⊥ shows the misfit dislocation [181].

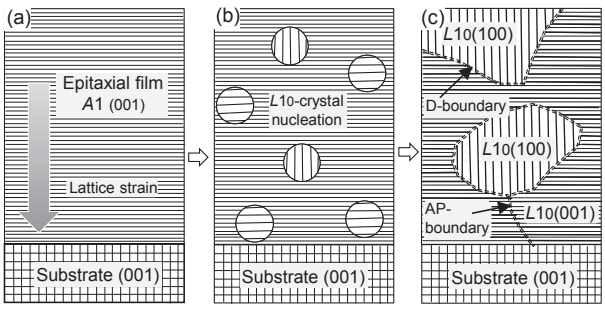

Fig. 18 Schematic model to explain the nucleation and growth of $L1_0$-crystal variants in disordered $A1$ phase matrix. (a) Lattice of $A1$ crystal epitaxially grown on MgO(001) substrate is strained to accommodate the lattice mismatch, where the $A1$ lattice is expanded in lateral direction whereas it is contracted in vertical direction. (b) Nucleation of $L1_0$-crystal is influenced by the $A1$ lattice strain. $L1_0$(001) crystal with $c/a < 1$ will be formed preferentially in a region close to the substrate interface while a more isotropic nucleation will take place in a region away from the interface. (c) Coalescence of growing crystal variants forms domain boundaries (D-boundary). Neighboring $L1_0$(001) crystals with a half-pitch difference (d_{002}) in the atomic stacking forms an anti-phase boundary (AP-boundary) [181].

diffusion across the interface of the two layers. These experimental results indicate that the lattice misfit of magnetic material with respect to the substrate, the underlayer, or the interlayer plays important roles in determining the variant orientation as well as the degree of $L1_0$ ordering.

The structure variation from $A1$ to $L1_0$ phase was investigated by XRD and HRTEM observations for FePt and FePd films on MgO(001) substrates as a function of film thickness to study the $L1_0$ variant crystal growth mechanism [181]. The results indicate that the resulting $L1_0$-variant structures are related with the degree of

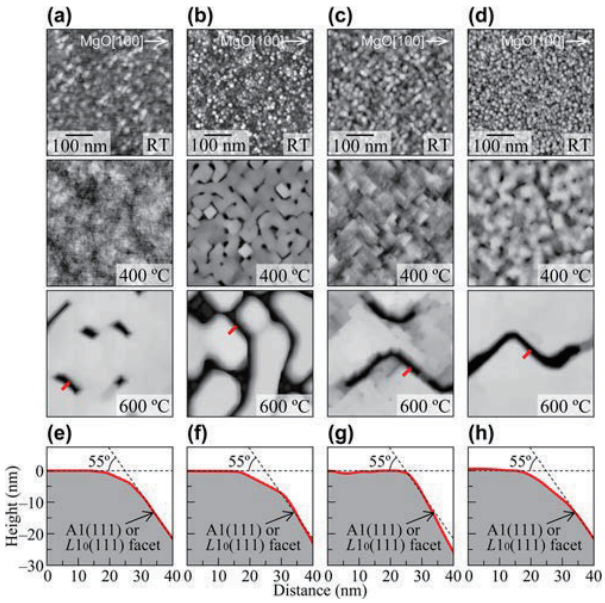

Fig. 19 AFM images of (a) FePt, (b) FePd, (c) CoPt, and (d) CoPd films grown at different substrate temperatures. (e)–(h) Cross-sectional profiles along the red lines in (a)–(d), respectively [185].

lateral lattice strain existing in the $A1$ phase film and that the preferential formation of $L1_0$(001) variant is due to larger lattice strains in the FePd film compared with the case of FePt film.

The effects of lateral lattice strain on $L1_0$-ordering were also studied for 10-nm-thick FePt films deposited on (001) oriented oxide single crystal substrates of MgO, $MgAl_2O_4$, $SrTiO_3$, and $LaAlO_3$ at a low substrate temperature of 200 °C and then annealed at 600 ° C [183], where the lattice mismatch of $A1$-FePt crystal with respect to the substrate ranged from -9.8% to +1.0%. Higher $L1_0$-ordering degree, S, is observed as MgO > $MgAl_2O_4$ > $SrTiO_3$ > $LaAlO_3$. The XRD and HRTEM study has shown that the lattice strain existing in the disordered ($A1$) film decreases during the high temperature $L1_0$-ordering process through introduction of misfit dislocations. The net misfit between $L1_0$-crystal and MgO(001) substrate is estimated to be less than 0.5% for the $L1_0$-ordered film. Figure 17 is an example of interface structure of $L1_0$-ordered Fe(Pt,Pd) epitaxial film formed on MgO(001) substrate. From the distributions of variant domain boundaries observed by HRTEM, the variant size is estimated to be 2 - 5 nm in diameter. A nucleation and growth model for explaining the $L1_0$-variant structure formation mechanism shown in Fig. 18 suggests a possibility in tailoring the variant structure in $L1_0$-ordered magnetic thin films by controlling the alloy composition, the layer structure, and the substrate material.

(b) Reduction of surface roughness for $L1_0$-ordered magnetic thin films

When a magnetic material is deposited on a

substrate, atom migration, adhesion to the substrate surface, and formation of three-dimensional clusters take place. The film growth mode depends basically on a difference between the binding energy of deposited atoms, E_f, and the energy to bond to the substrate, E_{fs}. In a case $E_{fs} > E_f$, the film growth takes place with the Frank-van der Merwe growth mode or the layer by layer mode, whereas the film growth follows the Volmer-Weber growth mode or the island-type growth mode for $E_{fs} < E_f$ [184]. Most of the combinations of magnetic materials (FePt, FePd, CoPt) and oxide substrates belong to the latter case. However, as the migration and diffusion behaviors of deposited atoms are influenced by the film formation process such as the deposition method and the substrate temperature, the resulting film nanostructure varies depending on these conditions, primarily on the substrate temperature. Figure 19 shows the variation of surface profiles observed for 40 nm-thick FePt, FePd, CoPt, and CoPd films deposited on MgO(001) substrates at RT, 400 °C, and 600 °C. Epitaxial growth is realized for all the films [185]. The nm-scale film surface undulations are caused by the atomic movements reflecting the surface energy variations of crystal facet as schematically illustrated in Fig. 19 (e)-(h). When the substrate temperature is lower than 200 °C, the films are continuous with relatively smooth surfaces. The arithmetical mean surface roughness, R_a, values for these films are less than 2 nm. However, with increasing the substrate temperature, the surface roughness increases to be larger than 10 nm and deep crevices are observed for the $L1_0$ ordered films prepared at 600 °C, which are caused by clustering of deposited magnetic material and consisting of facetted surfaces. Surface roughness caused by clustering at elevated substrate temperatures is noted for the $L1_0$-(001) oriented polycrystalline thin film media [186-188].

Considering that the film morphology is influenced during the film deposition process, a two-step process technique consisting of a low temperature film deposition followed by a high temperature annealing for $L1_0$ ordering has been investigated to prepare an $L1_0$ ordered film with improved surface flatness [153, 174, 175, 177]. Figure 20 compares the surface structures of FePd thin films of 2 - 40 nm thicknesses observed by atomic force microscopy (AFM). The films were deposited on MgO(001) substrates at 200 °C and then annealed at 600 °C. Smooth and continuous surface structures are realized for the films with thickness larger than 5 nm, showing an effectiveness of the two-step technique for the preparation of flat thin films. The surface roughness R_a of 40 nm-thick film prepared by employing the technique is as small as 0.15 - 0.3 nm. On the contrary, isolated island-like cluster structures are observed for the films thinner than 2 nm, where a clustering force of Fe and Pd atoms has apparently overcome the lateral binding force in the film. The degrees of $L1_0$ ordering in the films prepared by using the two-step method are similar to those of films directly deposited at 600 °C [180].

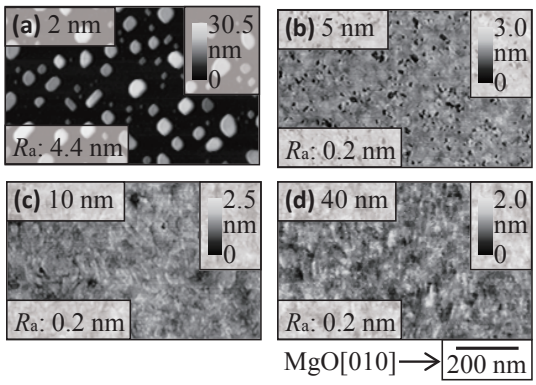

Fig. 20 AFM images of $L1_0$ ordered FePd films with (a) 2, (b) 5, (c) 10, and (d) 40 nm thicknesses prepared on MgO (001) substrates by deposition at 200 °C followed by annealing at 600 °C [175].

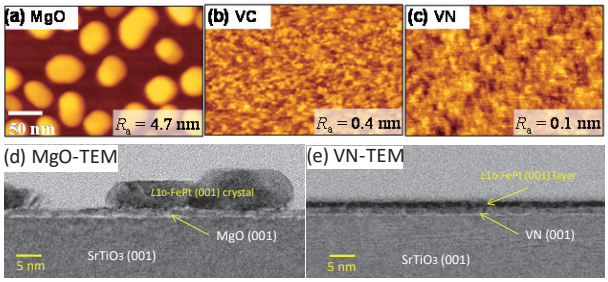

Fig. 21 AFM images of $L1_0$-FePt thin films of 2 nm in average thickness formed on (a) MgO, (b) VC, and (c) VN epitaxial underlayers [189]. (d) Cross-sectional TEM image of $L1_0$-FePt film of 2-nm average thickness formed on MgO layer and (e) cross-sectional TEM of 2-nm thick $L1_0$-FePt film formed on VN epitaxial layer. (a) (d) and (c) (e) images are for the same samples, respectively.

Although the two-step method is useful for the preparation of $L1_0$-ordered thin film with a flat and continuous surface down to a thickness around several nanometers, island-like isolated crystals are formed when the thickness is further decreased. In order to prepare a continuous thin film, the energy balance working on an isolated island needs to be considered. As a deposited material behaves like a liquid droplet on the substrate surface at high temperatures, the contact angle of island to the substrate surface is determined by a balance working between the surface energies of substrate (γ_{SG}), deposited material (γ_{LG}), and interfacial energy between these materials (γ_{SL}), which is known as Young relationship [189]. For achieving a lower contact angle, the condition, $\gamma_{SG} > \gamma_{SL} + \gamma_{LG}$, must be satisfied. Thus it seems useful to employ a substrate material of which surface energy is larger than that of magnetic material (FePt, FePd, CoPt). Figure 21 compares the morphology of $L1_0$-FePt(001) films of 2 nm average thickness formed on MgO (γ_{SG} = 1.4 J/m^2), VC (2.8 J/m^2), and VN (2-3 J/m^2) single-crystal underlayers of (001) orientation by employing the two-step method [190]. The

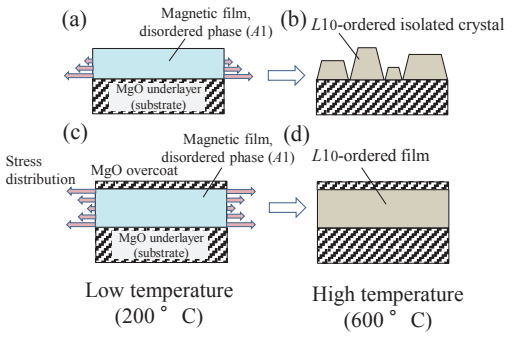

Fig. 22 Schematic model of $L1_0$ ordering from disordered structure, $A1$, magnetic film without overcoat (a), (b) and with overcoat (c), (d) epitaxially grown on MgO(001) substrate at low temperature (200 °C) followed by high temperature annealing (600 °C). The overcoat prevents clustering of magnetic material during the annealing process, thus providing a smooth surface of $L1_0$-ordered film. The order degree, S, is higher for the film with overcoat than that without overcoat [190, 191]

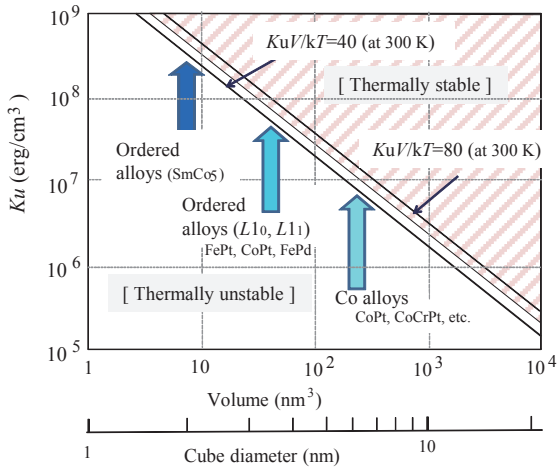

Fig. 23 Relationship between K_u and magnetic crystal grain volume for keeping the thermal stability condition, $K_uV/k_BT > 40 - 80$[126].

underlayer materials have a common NaCl-type crystal structure with similar lattice constants of 0.41 - 0.42 nm and $L1_0$-FePt crystal grows epitaxially with the c-axis perpendicular to the substrate surface. Very flat and continuous films with the surface roughness, $R_a < 0.4$ nm, are formed on the VC and VN underlayers, whereas isolated $L1_0$-FePt islands are formed on the MgO underlayer ($R_a = 4.2$ nm). An employment of underlayer material which has a surface energy larger than that of magnetic material seems to be crucial for the preparation of $L1_0$-ordered continuous magnetic thin films with very flat surfaces.

An another possibility to prepare $L1_0$(001) oriented magnetic thin films with flat surfaces is an employment of a thin overcoat on top of the magnetic thin film prepared by using the two-step method [191, 192]. A thin overcoat, 2 nm thick MgO layer was formed at 200 °C on FePt/MgO(001) samples with different FePt film thicknesses before annealing at 600 °C. Very flat and continuous surfaces with the R_a values less than 0.5 nm were realized for the 1-10 nm thick $L1_0$(001) FePt epitaxial thin films. Here the overcoat is interpreted to have worked in suppressing the atomic movements in the surface region of magnetic film during the high temperature ordering process at 600 °C preventing a formation of clusters. Furthermore, higher order degrees are also observed for the magnetic films with the MgO overcoats compared with the values of films of same thickness without overcoats. Formation of MgO overcoat layer is effective also in enhancing $L1_0$ ordering providing a lateral tension force to the magnetic layer from the surface side. Figure 22 shows a schematic model explaining the effect of overcoat. The basic findings obtained from the experimental studies employing $L1_0$ epitaxial thin films are believed to be useful in tailoring the high K_u $L1_0$ magnetic thin films to be applied for practical recording media.

7. Future possibilities of high K_u magnetic materials

In order to apply the high K_u magnetic materials with $L1_0$ ordered structure for PMR media, practical technologies in tuning the nanostructure such as magnetic crystal grain isolation, high $L1_0$ ordering within a small crystal grain, appropriate control of grain size, narrow distribution of grain size, etc. while adjusting the magnetic properties, need to be developed. In addition, surface flatness and mechanical durability conditions that are related with very narrow physical spacing of less than a few nanometers between a magnetic head and a medium must be simultaneously satisfied. The development of such a highly sophisticated technology is a big challenge. However, the authors believe it will be possible likewise the past developments of media technology that enabled a dramatic areal density growth of HDD through intensive experiments carried out based on the basic science of materials.

Thermal stability of recorded information depends on $K_u V/k_B T$. When T is room temperature (300 K), the relation between magnetic crystal grain volume V (nm^3) and K_u (erg/cm^3) for maintaining the thermal stability is plotted as shown in Fig. 23 [2, 126]. Assuming the magnetic grain to be a cube shape, the cube edge length is also indicated as a measure in the figure. To decrease the length while keeping the thermal stability $K_u V/k_B T > 60$, K_u must be increased from the order of 10^6 erg/cm^3 which is with the Co-alloy materials currently employed as PMR media, to the order of 10^7 erg/cm^3 or higher. Although there are more than several magnetic materials with the K_u values higher than 10^7 erg/cm^3 as explained before, $L1_0$-ordered magnetic alloy materials seem to be the practical candidate for future PMR media because of the excellent chemical stability and the higher potential in tuning the nanometer level structure. The

minimum edge length of cube crystal for keeping the thermal stability is calculated to be 3.4 nm for the $L1_0$-ordered FePt material which possesses the K_u value 6.6 $\times 10^7$ erg/cm^3 [129]. Assuming a physical separation of 0.5 nm between magnetic crystals, the areal density will be increased up to around 40 Tb/in^2. If a $SmCo_5$ crystal with the K_u value of 2×10^8 erg/cm^3 is applied, an areal density of more than 80 Tb/in^2 seems feasible. From thermal stability and available magnetic material points of view, an areal density of 100 Tb/in^2 which is more than 100 times larger than that of current areal density seems to be achievable by carefully tuning the sub-nanometer level structure of high K_u magnetic materials.

8. Summary

The developments of perpendicular magnetic recording media technology are briefly reviewed from a view point in tailoring the nanostructure of recording layer. Before establishing the PMR media structure that employs the granular-type Co-alloy recording layer with an hcp structure, there was a long history of research and development (R&D) since the invention of PMR in 1976. Including the early stage of R&D of Co-alloy recording layer, the technological developments in aligning the easy magnetization axis by hetero-epitaxial thin film growth and in achieving magnetic separation between the magnetic crystal grains by nonmagnetic elements segregation around the grain boundaries are explained. It is also shown that observations of composition and magnetization structures have played key roles for the improvement of medium nanostructure to be tuned suitable for high density magnetic recording.

Although Co-alloy recording layer materials have been used since the invention of PMR and will be continuously used up to an areal density beyond 1 Tb/in^2 by adding further tunings to the medium structure and possibly through a technological modification in the recording scheme [21, 22, 161], an employment of high K_u magnetic material is necessary for the recording layer in keeping the thermal stability of recorded information for further increasing the areal density well beyond 2 - 3 Tb/in^2. However, an employment of high K_u magnetic material brings in new technological issues which are different from those associated with conventional Co-alloy materials. From such viewpoints, basic research results related with technologies in controlling the easy magnetization and in keeping the surface flatness for $L1_0$-ordered magnetic thin films are also briefly explained. Finally, future possibilities of PMR media materials are discussed from the thermal stability of recorded information and the available magnetic material points of view. The authors believe that an areal density of 100 Tb/in^2 which is more than 100 times larger than that of current areal density seems to be achievable by carefully tuning the sub-nanometer level structure of magnetic materials.

Acknowledgements

The author (M. F.) would like to thank the colleagues at Hitachi CRL who worked with the author during "the dip period" lasted for 10 - 15 years, and the members of the committee 144 of the Japan Society for the Promotion of Science who worked toward the realization of PMR-HDDs, of which names are listed as the reference paper authors. The authors also thank the students of Chuo University who patiently collected valuable scientific data.

References

1) S. Iwasaki and Y. Nakamura: *IEEE Trans. Magn.*, **MAG-13**, 1272 (1977).
2) M. Futamoto: *IEICE Technical Report*, **MR2014-5**, 25 (2014).
3) Y. Uesaka, M. Koizumi, N. Tsumita, O. Kitakami, and H. Fujiwara: *J. Appl. Phys.,* **57** (1985) 3925.
4) W. Cain, A. Payne, M. Baldwinson, and R. Hempstead: *IEEE Trans. Magn.,* **32**, 97 (1996).
5) M. Oshiki: J. Mag. Soc. Japan., **21**, suppl. S1, 91 (1996).
6) D. A. Thompson: *J. Mag. Soc. Japan*, **21**, Suppl. S2, 9 (1997).
7) P-L. Lu and S. H. Charap: *IEEE Trans. Magn.*, **30**, 4230 (1994).
8) Y. Hosoe, I. Tamai, K. Takahashi, Y. Tanahashi, T. Yamamoto, T. Kanbe, and Y. Yajima: *IEEE Trans. Magn.,* **33**, 3028 (1997).
9) M. Futamoto, Y. Hirayama, N. Inaba, Y. Honda, K. Ito, A. Kikukawa, and T. Takeuchi: *IEEE Trans. Magn.* **35**, 2802 (1999).
10) H. Takano, Y. Nishida, M. Futamoto, H. Aoi, and Y. Nakamura: *Abstract of Intermag 2000*, AD-06.
11) T. Ando and T. Nishikawa: *IEEE Trans. Magn.,* **33**, 2983 (1997).
12) M. Futamoto, Y. Hirayama, Y. Honda, A. Kikukawa, K. Tanahashi, and A. Ishikawa: *J. Mag. Mag. Mater.*, **235**, 281 (2001).
13) K. Tanahashi, N. Shimizu, A. Kikukawa, Y. Honda, A. Ishikawa, and M. Futamoto: *J. Mag. Mag. Mater.*, **235**, 59 (2001).
14) Y. Kawato, M. Futamoto, and K. Nakamoto: *U. S. Patent*, US2002/0 028356A1 (2002).
15) M. J. Carey, Y. Ikeda, S. Smith, and K. Takano: *U.S. Patent* US2003/0 022 023 A1 (2003).
16) S. C. Byeon, A. Misra, and W. D. Doyle: *IEEE Trans. Magn.*, **40**, 2386 (2004).
17) S. Oikawa, A. Takeo, T. Hikosaka, and Y. Tanaka: *IEEE Trans. Magn.*, **36**, 2393 (2000).
18) Y. Tanaka and T. Hikosaka: *J. Mag. Mag. Mater.*, **235**, 253 (2001).
19) http://www.toshiba.co.jp/about/press/2004_12/pr1401.htm
20) Y. Tanaka: *Proc. IEEE*, **96**, 1754 (2008).
21) Y. Shiroishi, K. Fukuda, I. Tagawa, H. Iwasaki, S. Takenori, H. Tanaka, H. Mutoh, and N. Yoshikawa: *IEEE Trans. Magn.*, **45**, 3816 (2009).
22) A. Kikitsu, T. Maeda, H. Hieda, R. Yamamoto, N. Kihara, and Y. Kamata: *IEEE Trans. Mag.*, **49**, 693 (2013).
23) S. Iwasaki and K. Ouchi: *IEEE Trans. Magn.*, **MAG-14**, 849 (1978).
24) M. Futamoto, Y. Honda, and H. Kakibayashi: *Japan. J. Appl. Phys.*, **24**, L460 (1985).
25) Y. Honda, M. Futamoto, K. Yoshida, Y. Uesaka, Y. Shiroishi, and H. Kakibayashi: *IEICE Trans.*, **J69-C**, 85 (1986).
26) Y. Honda, M. Futamoto, S. Saito, and K. Yoshida: *IEICE Trans.*, **73-C11**, 74 (1990).
27) H. S. Gill and T. Yamashita: *IEEE Trans. Magn.*, **MAG-20**, 776 (1984).
28) R. Sugita, K. Takahashi, K. Honda, K. Kanai, and F.

Kobayashi: *Digests of the 6th Annual Conference of Magnetics in Japan*, pp.42 (1982).
29) H. S. Gill and M. P. Rosenblum: *IEEE Trans. Magn.*, **MAG-19**, 1644 (1983).
30) M. Futamoto, H. Honda, H. Kakibayashi, and K. Yoshida: *IEEE Trans. Magn.*, **MAG-21**, 1426 (1985).
31) P. W. Jong, Y. H. Kim, T. D. Lee, and T. Kang: *IEEE Trans. Magn.*, **25**, 4168 (1989).
32) Y. Hirayama and M. Futamoto: *J. Mag. Soc. Japan*, **19**, Suppl. No. S2, 14 (1995).
33) K. H. Krishnan, T. Takeuchi, Y. Hirayama, and M. Futamoto: *IEEE Trans. Magn.*, **30**, 5115 (1991).
34) D. J. Mapps, G. Pan, and M. H. Akhter: *IEEE Trans. Magn.*, **27**, 4168 (1991).
35) X. Song, J. Loven, J. Sivertsen, and J. Judy: *IEEE Trans. Magn.*, **32**, 3840 (1996).
36) M. Futamoto, Y. Honda, and K. Yoshida: *Journal de physique,* **Colloque C8**, Suppl. 12, Tome 49, C8-1979 (1988).
37) Y. Matsuda, M. Suzuki, Y. Hirayama, and M. Futamoto: *J. Mag. Soc. Japan*, **18**, suppl. No. S1, 99 (1994).
38) Y. Hirayama, M. Futamoto, K. Ito, Y. Honda, and Y. Maruyama: *IEEE Trans. Magn.*, **33**, 996 (1997).
39) A. Sato, S. Nakagawa, and M. Naoe: *IEEE Trans. Magn.*, **36**, 2387 (2000).
40) J. Ariake, N. Honda, K. Ouchi, and S. Iwasaki: *J. Mag. Mag. Mater.*, **242-245**, 311 (2002).
41) M. Futamoto, Y. Hirayama, N. Inaba, Y. Honda, ans A. Kikukawa: *IEICE Trans.*, **E84-C**, 1132 (2001).
42) M. Zheng, G. Choe, K. E. Johnson, L. Gao, and S-H. Liou: *IEEE Trans. Magn.*, **38**, 3193 (2002).
43) W. K. Shen, A. Das, M. Racine, R. Cheng, J. H. Judy, and J-P. Wang: *IEEE Trans. Magn.*, **42**, 2945 (2006).
44) U. Kwon, R. Sinclair, E. M. T. Velu, S. Malhotra, and G. Bertero: *IEEE Trans. Magn.*, **41**, 3193 (2005).
45) M. Futamoto, Y. Hirayama, Y. Honda, K. Ito, and K. Yoshida: *J. Mag. Soc. Japan*, **21**, Suppl. No. S2, 141 (1997).
46) Y. Hirayama, A. Kikukawa, Y. Honda, N. Shimizu, and M. Futamoto: *IEEE Trans. Magn.*, **36**, 2396 (2000).
47) M. Futamoto, Y. Hirayama, Y. Honda, and N. Inaba: *J. Mag. Mag. Mater.*, **226-230**, 1610 (2001).
48) M. Futamoto: *J. Optoelectron. Adv. Mater.*, **8**, 1861 (2006).
49) M. Futamoto, K. Terayama, K. Sato, and Y. Hirayama: *IEICE, Trans. Electron.*, **E85-C**, 1733 (2002).
50) M. Futamoto, K. Terayama, K. Sato, and Y. Hirayama: *Scr. Mater.*, **42**, 929 (2003).
51)W. Sucksmith and J. E. Thompson: Proc. *Roy. Soc. London*, Ser. A, **225**, 362 (1954).
52) Y. Takahashi, K. Tanahashi, and Y. Hosoe: J. Appl. Phys., **91**, 8022 (2002).
53) S. Saito, S. Hinata, and M. Takahashi: *IEEE Trans. Magn.*, **50**, 3201205 (2014).
54) K. Yoshida, H. Kakibayashi1 and H. Yasuoka: *J. Appl. Phys.*, **68**, 705 (1990).
55) J. O. Artman: J. Appl. Phys., **61**, 3137 (1987).
56) Y. Maeda, S. Hirono, and M. Asahi: Japan. *J. Appl. Phys.*, **24**, L951 (1985).
57) Y. Maeda and M. Asahi: *J. Appl. Phys.*, **61**, 1972 (1987).
58) H. Suzuki, N. Goda, S. Nagaike, Y. Shiroishi, N. Shige, and N. Tsumita: *IEEE Trans. Magn.*, **27**, 4718 (1991).
59) J .N. Chapman, I. R. McFadyen, and J. P. C. Bernards: *J. Mag. Mag. Mater.*, **62**, 359 (1986).
60) D. I. Rogers, J. N. Chapman, J. P. C. Bcrnalds, and S. B. Luitjens: *IEEE Trans. Magn.*, **25**, 4180 (1989).
61) H. Aoi, F. Tomiyama, Y. Shiroishi, K. Yoshida, and Y. Sugita: *IEEE Trans. Magn.*, **29**, 3715 (1993).
62) H. Aoi, F. Kugiya, R. Tsuchiya, and M. Suzuki: *IEEE Trans. J. Mag. Japan*, **4**, 164 (1989).
63) M. Futamoto: *Tech. Rep. IEICE*, **MR94-81**, 53 (1995).
64) M. Futamoto, N. Inaba, Y. Hrayama, K. Kimoto, and K. Usami: *Tech. Rep. IEICE*, **MR95-49**, 35 (1995).
65) Y. Yahisa, K. Kimoto, K. Usami, Y. Matsuda, J. Inagaki, K. Furusawa, and S. Narishige: *IEEE Trans. Magn.*, **31**, 2836 (1995).
66) Y. Hirayama, M. Futamoto, K. Kimoto, and K. Usami: *IEEE Trans. Magn.*, **32**, 3807 (1996).
67) K. Kimoto, Y. Hirayama, and M. Futamoto: *J. Mag. Mag. Mater.*, **159**, 401 (1996).
68) J. Nakai, A. Kikuchi, M. Kuwabara, T. Sakurai, T. Shimatsu, and M. Takahashi: *IEEE Trans. Magn.*, **31**, 2833 (1995).
69) M. Takahashi, A. Kikuchi, H. Hara, and H. Shoji: *IEEE Trans. Magn.*, **34**, 1573 (1998).
70) M. Futamoto, Y. Honda, and K. Yoshida: *J. Mag. Mag. Mater.*, **74**, 134 (1988).
71) M. Futamoto, Y. Hirayama, Y. Honda, and A. Kikukawa: *NATO Science Series* "Magnetic Storage Systems beyond 2000" ed. by G. C. Hadjipanayis, p. 103, (Kluwer Acad. Pub., Netherlands, 2001).
72) Y. Hirayama, K. Ito, Y. Honda, N. Inaba, and M. Futamoto: *J. Mag. Mag. Mater.*, **193**, 253 (1999).
73) N. Inaba, Y. Uesaka, and M. Futamoto: *IEEE Trans. Magn.*, **36**, 54 (2000).
74) P. F. Carcia, A. D. Meinhaldt, and A. Suna: *Appl. Phys. Lett.*, **47**, 178 (1985).
75) M. Suzuki, H. Awano, N. Inaba, Y. Honda, and M. Futamoto: *J. Mag. Soc. Japan*, **18**, Suppl. No. S1, 451 (1994).
76) B. M. Lairson, J. Perez, and C. Baldwin: *IEEE Trans. Magn.*, **30**, 4014 (1994).
77) L. Wu, N. Honda, and K. Ouchi: *IEEE Trans. Magn.*, **35**, 2775 (1999).
78) Y. Kubota, D. Weller, M-L. Wu, X. Wu, G. Ju, D. Karns, and J. Yu: *J. Mag. Mag. Mater.*, **242-245**, 297 (2002).
79) S. Matsunuma, A. Yano, T. Koda, T. Onuma, H. Yamanaka, and E. Fujita: *IEEE Trans. Magn.*, **40**, 2492 (2004).
80) Y. Ota, N. Tani, M. Ishikawa, T. Yamada, K. Nakamura and A. Itoh: *IEEE Trans. Magn.*, **MAG-20**, 768 (1984).
81) T. Sato and T. Kitamura: *IEEE Trans. J. Mag. Japan*, **TJMJ-1**, 765 (1985).
82) K. Yoshida and T. Takayama: *J. Mag. Mag. Mater.*, **82**, 228 (1989).
83) T. Hikosaka, T. Komai, and Y. Tanaka: *IEEE Trans. Magn.*, **30**, 4026 (1994).
84) Y. Tanaka and T. Hikosaka: *J. Magn. Magn. Mater.*, **235**, 253 (2001).
85) A. Takeo, S. Oikawa, T. Hikosaka, and Y. Tanaka: *IEEE Trans. Magn.*, **36**, 2378 (2000).
86) Y. Tanaka: *IEEE Trans. Magn.*, **41**, 2834 (2005).
87) T. Handa, Y. Takahashi, R. Araki, and M. Futamoto: *J. Mag. Soc. Japan*, **32**, 260 (2008).
88) M. Futamoto, T. Handa, and Y. Takahashi: *IEEE Trans. Magn.*, **44**, 3488 (2008).
89) M. Futamoto, T. Handa, and Y. Takahashi: *J. Phys. Conf. Ser.*, **200**, 102001 (2010).
90) H. Weinforth, Ch. Somsen, B. Rellinghaus, A. Carl, E. F. Wassermann, and D. Weller: *IEEE Trans. Magn.*, **34**, 1132 (1998).
91) T. Oikawa, M. Nakamura, H. Uwazumi, T. Shimatsu, H. Muraoka, and Y. Nakamura: *IEEE Trans. Magn.*, **38**, 1976 (2002).
92) J. Ariake, T. Chiba, and N. Honda: *IEEE Trans. Magn.*, **41**, 3142 (2005).
93) T. Chiba, J. Ariake, and N. Honda: *J. Mag. Mag. Mater.*, **287**, 167 (2005).
94) S. Iwasaki, Y. Nakamura, and K. Ouchi: *IEEE Trans. Magn.*, **MAG-15**, 1456 (1979).
95) S. B. Luitjens, C. P. G. Schrauwen, J. P. C. Bernards, and V. Zieren: *IEEE Trans. Magn.*, **MAG-21**, 1438 (1985).
96) T. Ando and T. Nishihara: *J. Mag. Soc. Japan*, **15**, Suppl. S2, 1019 (1991).
97) Y. Honda, K. Tanahashi, Y. Hirayama, A. Kikukawa, and M. Futamoto: *IEEE Trans. Magn.*, **37**, 1315 (2001).

98) Y. Honda, A. Kikukawa, Y. Hirayama, and M. Futamoto:, *IEEE Trans. Magn.*, **36**, 2399 (2000).
99) A. Kikukawa, Y. Honda, Y. Hirayama, and M. Futamoto: *IEEE Trans. Magn.*, **36**, 2402 (2000).
100) A. Kikukawa, K. Tanahashi, Y. Honda, Y. Hirayama, and M. Futamoto: *IEEE Trans. Magn.*, **37**, 1602 (2001).
101) R. Mukai, T. Uzumaki, and A. Tanaka: *IEEE Trans. Magn.,* **41**, 3169 (2005).
102) K. Tang, X. Bian, G. Choe, K. Takano, M. Mirzamaani, G. Wang, J. Zhang, Q.-F. Xiao, Y. Ikeda, J. R. Jamtgaard, and X. Xu: IEEE Trans. Magn., 45, 786 (2009).
103) J. A. Thornson: *J. Vac. Sci. Technol.*, **A4** (6), 3059 (1986).
104) Y. Sonobe, H. Muraoka, K. Miura, Y. Nakamura, K. Takano, A. Moser, H. Do, B. K. Yen, Y. Ikeda, N. Supper, and W. Weresin: *IEEE Trans. Magn.*, **38**, 2006 (2002).
105) Y. Sonobe, K. K. Tham, L. Wu, T. Umezawa, C. Takasu, J. A. H. Dumaya, T. Onoue, P. Leo, and M. Liau: *IEEE Trans. Magn.*, **42**, 2351 (2006).
106) Y. Honda, M. Futamoto, T. Kawasaki, K. Yoshida, M. Koizumi, F. Kugiya, and A. Tonomura: *Japan. J. Appl. Phys.*, **26**, L923 (1987).
107) K. Yoshida, Y. Honda, T. Kawasaki, M. Koizumi, F. Kugiya, M. Futamoto, and A. Tonomura: *IEEE Trans. Magn.*, **MAG-23**, 2073 (1987).
108) K. Yoshida, Y. Honda, M. Futamoto, T. Kawasaki, S. Hasegawa, and A. Tonomura: *J. Mag. Soc. Japan*, **15**, Suppl. No. S2, 463 (1991).
109) K. Ouchi and S. Iwasaki: *IEEE Trans. Magn.*, **MAG-18**, 1110 (1982).
110) T. Kohashi, M. Konoto, A. Nakamura, R. Araki, and K. Koike: *Digest of Intermag 2006*, HD-04 (2006).
111) J. P. C. Bernards and A. J. den Boef: *IEEE Trans. Magn.*, **26**, 1515 (1990).
112) Y. Honda, S. Hosaka, A. Kikukawa, S. Tanaka, Y. Matsuda, M. Suzuki, and M. Futamoto: *Japan. J. Appl. Phys.*, **31**, L1061 (1992).
113) M. Futamoto and Y. Honda: *J. Mag. Soc. Japan*, **18**, Suppl. No. S1, 485 (1994).
114) G. Binning, C. F. Quate, Ch. Gerber: *Phys. Rev. Lett.*, **56**, 930 (1986).
115) K. Nagano, K. Tobari, K. Soneta, M. Ohtake, and M. Futamoto: *J. Mag. Soc. Japan*, **36**, 109 (2012).
116) M. Futamoto, T. Hagami, S. Ishihara, K. Soneta, and M. Ohtake: *Key Eng. Mater.*, **543**, 35 (2013).
117) S. Ishihara, M. Ohtake, and M. Futamoto: *J. Mag. Soc. Japan*, **37**, 255 (2013).
118) M. Futamoto, T. Hagami, S. Ishihara, K. Soneta, and M. Ohtake: *IEEE Trans. Magn.*, **49**, 2748 (2013).
119) M. Futamoto and M. Ohtake: *Key Eng. Mater.*, **644**, 189 (2015).
120) L. Gao, L. P. Yue, T. Yokota, R. Skomski, S. H. Liou, H. Takahoshi, H. Saito, and S. Ishio: *IEEE Trans. Magn.*, **40**, 2194 (2004).
121) N. Amos, A. Lavrenov, R. Fernandez, R. Ikkawi, D. Litvinov, and S. Khizroev: *J. Appl. Phys.*, **105**, 07D526 (2009).
122) W. Lu, Z. Li, K. Hatakeyama, G. Egawa, S. Yoshimura, and H. Saito: *J. Appl. Phys.*, **96**, 143104 (2010).
123) K. Soneta, M. Ohtake, and M. Futamoto: *J. Mag. Soc. Japan*, **37**, 107 (2013).
124) T. Hagami, M. Ohtake, and M. Futamoto: *J. Mag. Soc. Japan*, 37, 231 (2013).
125) S. Ishihara, M. Ohtake, and M. Futamoto: *EPJ Web Conf.*, **40**, 01002, (2013).
126) M. Futamoto: *ECS Trans.*, **50**, 59 (2013).
127) T. Suzuki, N. Honda, and K. Ouchi: *Tech. Rept. IEICE*, **MR97-16**, 53 (1997)
128) D. Weller and A. Moser: *IEEE Trans. Magn.*, **35**, 4423 (1999).
129) T. Burkert, L. Nordström, O. Eriksson, and O. Heinonen: *Phys. Rev. Lett.*, **93**, 027203 (2004).
130) Y. Nukaga, M. Ohtake, F. Kirino, and M. Futamoto: *IEEE Trans. Magn.*, **44**, 2891 (2008).
131) M. Ohtake, Y. Nukaga, F. Kirino, and M. Futamoto: *J. Appl. Phys.*, **105**, 07C315 (2009).
132) O. Yabuhara, M. Ohtake, Y. Nukaga, F. Kirino, and M. Futamoto: *J. Phys. Conf. Ser.*, **200**, 082026 (2010).
133) M. Ohtake, O. Yabuhara, Y. Nukaga, F. Kirino, and M. Futamoto: *J. Appl. Phys.*, **107**, 09A708 (2010).
134) T. Yanagawa, M. Ohtake, F. Kirino, and M. Futamoto: *EPJ Web Conf.*, **40**, 06007 (2013).
135) M. Yamada, Y. Hotta, T. Yanagawa, M. Ohtake, F. Kirino, and M. Futamoto: *IEEE Trans. Magn.*, **50**, 2101604 (2014).
136) M. Yamada, T. Yanagawa, Y. Hotta, M. Ohtake, F. Kirino, and M. Futamoto: *EPJ Web Conf.*, **75**, 04010 (2014).
137) M. Yamada, Y. Hotta, A. Suzuki, M. Ohtake, M. Futamoto, F. Kirino, and N. Inaba: *Digest 38th Conf. Mag. Soc. Japan*, 2aB-03, p.18 (2014).
138) M. Seifert, V. Neu, and L. Schultz: *Appl. Phys. Lett.*, **94**, 022501 (2009).
139) M. Ohtake, Y. Nukaga, F. Kirino, and M. Futamoto: *J. Cryst. Growth*, **311**, 2251 (2009).
140) B. N. Engel, C. D. England, R. A. Van Leeuwen, M. H. Wiedmann, and C. M. Falco: *Phys. Rev. Lett.*, **67**, 1910 (1991).
141) H. Ohmori and A. Maesaka: *J. Mag. Soc. Japan.*, **26**, 224 (2002).
142) K. Tobari, M. Ohtake, K. Nagano, and M. Futamoto: Japan. *J. Appl. Phys.*, **50**, 073001 (2011).
143) K. Tobari , M. Ohtake, K. Nagano, and M. Futamoto: *Thin Solid Films*, **519**, 8384 (2011).
144) K. Tobari, M. Ohtake, K. Nagano, and M. Futamoto: *J. Mag. Mag. Mater.*, **324**, 1059 (2012).
145) M. Ohtake, K. Tobari, and M. Futamoto: *IEICE Trans. Electron.*, **E96-C**, 1452 (2013).
146) H. Okamoto: Phase Diagrams for Binary Alloys, p. 255 (Materials Park, OH, ASM International, 2000).
147) S. Iwata, S. Yamashita, and S. Tsunashima: *IEEE Trans. Magn.*, **32**, 3670 (1997).
148) G. F. Hughes: Patterned Media in "The Physics of Ultra-High-Density Magnetic Recording", p. 205 (Springer, New York, 2002).
149) E. Suharyadi, S. Natsume, T. Kato, S. Tsunashima, and S. Iwata: *Trans. Magn. Soc, Japan*, **5**, 125 (2005).
150) K. Takenaka, N. Saidoh, N. Nishiyama, M. Ishimaru, M. Futamoto, and A. Inoue: *J. Mag. Mag. Mater.*, **324**, 1444 (2012).
151) S. Chikazumi et al. ed.: Handbook of Magnetic Materials, (Asakura Shoten, Tokyo, 2006).
152) J. M. D. Coey: Magnetism and Magnetic Materials, (Chambridge University Press, New York, 2009).
153) A. Itabashi, M. Ohtake, F. Kirino, and M. Futamoto: *IEICE Tech. Rept.*, **MR2013-7**, 7 (2013).
154) Z. L. Jun, N. S. Hua, and Z. J. Hua: *ArXiv* 1309.0298, pp.1-14 (2013).
155) R. S. Bandhu and R. Sooryakumar, R. F. C Farrow, D. Weller, M. F. Toney, and T. A. Rabedeau: *J. Appl. Phys.*, **91**, 2737 (2002)
156) G. R. Harp, D. Weller, T. A. Rabedeau, R. F. C. Farrow, and M. F. Toney: *Phys. Rev. Lett.*, **71**, 2493 (1993).
157) T. Suzuki, N. Honda, and K. Ouchi: *J. Mag. Soc. Japan*, **21,** S2, 177 (1997).
158) T. Suzuki, T. Kiya, N. Honda, and K. Ouchi: *IEEE Trans. Magn.*, **36**, 2417 (2000).
159) T. Suzuki and K. Ouchi: *IEEE Trans. Magn.*, **37**, 1283 (2001).
160) D. E. Laughlin, S. Kumar, Y. Peng, and A. G. Roy: *IEEE Trans. Magn.*, **41**, 719 (2005).
161) D. Weller, G. Parker, O. Mosendz, E. Champion, B. Stipe, X. Wang, T. Klemmer, G. Ju, and A. Ajan: *IEEE Trans. Magn.*, **50**, 3100108 (2014).
162) D. Suzuki, M. Ohtake, F. Kirino, and M. Futamoto: *IEEE*

Trans. Magn., **48**, 3195 (2012).
163) M. Ohtake, S. Ouchi, F. Kirino , and M. Futamoto: *IEEE Trans. Magn.*, **48**, 3595 (2012).
164) D. Suzuki, M. Ohtake, S. Ouchi, F. Kirino, and M. Futamoto: *J. Mag. Soc. Japan*, **36**, 336 (2012).
165) D. Suzuki, M. Ohtake, F. Kirino, and M. Futamoto: *J. Mag. Soc. Japan*, **37**, 179 (2013).
166) M. Ohtake, D. Suzuki, F. Kirino, and M. Futamoto: *ECS Trans.*, **50**, 69 (2013).
167) D. Suzuki, M. Ohtake, F. Kirino, and M. Futamoto: *EPJ Web Conf.*, **40**, 11003 (2013).
168) M. Ohtake, D. Suzuki, F. Kirino, and M. Futamoto: *IEICE Trans. Electron.*, **E96-C**, 1460 (2013).
169) M. Ohtake, D. Suzuki, and M. Futamoto: *J. Appl. Phys.*, **115**, 17C116 (2014).
170) D. Suzuki, M. Ohtake, F. Kirino, and M. Futamoto: *J. Appl. Phys.*, **115**, 17C120 (2014).
171) M. Ohtake, D. Suzuki, F. Kirino, and M. Futamoto: *EPJ Web Conf.*, **75**, 06003 (2014).
172) M. Ohtake, D. Suzuki, M. Futamoto, F. Kirino, and N. Inaba: *J. Mag. Soc. Japan*, **39**, 15 (2015).
173) K. Sato, B. Bian, T. Hanada, and Y. Hirotsu: *Scripta Mater.*, **44**, 1389 (2001).
174) K. Sato, B. Bian, and Y. Hirotsu: *J. Appl. Phys.*, **91**, 8516 (2002).
175) A. Itabashi, M. Ohtake, S. Ouchi, F. Kirino, and M. Futamoto: *J. Mag. Soc. Japan*, **37**, 358 (2013).
176) Y. Numata, A. Itabashi, M. Phtake, F. Kirino, and M. Futamoto: *IEEE Trans. Magn.*, **50**, 210304 (2014).
177) A. Itabashi, M. Ohtake, S. Ouchi, F. Kirino, and M. Futamoto: *IEEE Trans. Magn.*, **48**, 3203 (2012).
178) A. Itabashi, M. Ohtake, F. Kirino, and M. Futamoto: *EPJ Web Conf.*, **75**, 06012 (2014).
179) M. Ohtake, A. Itabashi, M. Futamoto, F. Kirino, and N. Inaba: *Key Eng. Mater.*, **644**, 227 (2015).
180) M. Ohtake, A. Itabashi, M. Futamoto, F. Kirino, and N. Inaba: *IEEE Trans. Magn.*, **51**, 2100904 (2015).
181) M. Futamoto, M. Nakamura, M. Ohtake, N. Inaba, and T. Shimotsu: *AIP Adv.*, **6**, 085302 (2016).
182) Y. Numata, M. Ohtake, M. Futamoto, F. Kirino, and N. Inaba: *Abst. 38th Conf. Mag. Soc. Japan.*, 4aE-10, p.289 (2014).
183) M. Nakamura, R. Ochiai, M. Ohtake, M. Futamoto, F. Kirino, and N. Inaba: *IEICE Tech. Rep.,* **MR2016-14**, 7 (2016).
184) J. A. Venables: Introduction to Surface and Thin Film Processes, (Cambridge Univ. Press, Cambridge, 2000).
185) M. Ohtake, S. Ouchi, F. Kirino, and M. Futamoto: *J. Appl. Phys.*, **111**, 07A708 (2012).
186) L. S. Huang, J. F. Hu, G. M. Chow, and J. S. Chen: *J. Appl. Phys.*, **109**, 063910 (2011).
187) I. Takekuma, H. Nemoto, H. Matsumoto, S. Ito, J. Sayama, A. Hirotsune, and Y. Hirayama: *J. Appl. Phys.*, **111**, 07B708 (2012).
188) K. F. Dong, H. H. Li, Y. G. Peng, G. Ju, G. M. Chow, and J. S. Chen: *Appl. Phys. Lett.*, **104**, 192404 (2014).
189) T. Young: *Philos. Trans. R. Soc. Lond.*, **95**, 65 (1805).
190) T. Shimizu, M. Ohtake, M. Futamoto, F. Kirino, and N. Inaba, *IEEE Trans. Magn.* **53** (2017) (to appear).
191) M. Ohtake, A. Itabashi, M. Futamoto, F. Kirino, and N. Inaba: *J. Mag. Soc. Japan*, **39**, 167 (2015).
192) Y. Noguchi, M. Ohtake, M. Futamoto, and N. Inaba: *J. Mag. Mag. Mater.*, **410**, 81 (2016).

Received May 05, 2017; Revised June 28, 2017; Accepted August 17, 2017

J. Magn. Soc. Jpn., **41**, 127-131 (2017)

<Paper>

Synthesis and Magnetic Properties of ($Zn^{2+}Ti^{4+}$) Substituted W-type and Y-type Ferrites

K. Watanabe, K. Kakizaki, and K. Kamishima

Graduate School of Science and Engineering, Saitama University, *255 Shimo-Okubo, Sakura-ku, Saitama 338-8570, Japan*

We report the synthesis of ($Zn^{2+}Ti^{4+}$) substituted hexagonal ferrites, $BaZn_2(Zn_{0.5}Ti_{0.5})_xFe_{16-x}O_{27}$ (W-type) and $Ba_2Zn_2(Zn_{0.5}Ti_{0.5})_xFe_{12-x}O_{22}$ (Y-type), and the relationship between their composition and magnetic properties. Substituted W-type ferrite was synthesized in the region of $0.0 \leq x \leq 1.5$. A decrease in the Curie temperature of the W-type phase indicated that the exchange interactions between the Fe^{3+} ions weakened due to the substitution of Zn^{2+} and Ti^{4+} ions. Spontaneous magnetization (σ_S) at $x = 0.5$ was similar to that at $x = 0.0$. This reflects the equal distribution of nonmagnetic Zn^{2+} and Ti^{4+} ions to spin down sites and spin up sites, respectively. At $x > 0.5$, σ_S decreased clearly, which was possibly caused by a deviation from the collinear arrangement. Substituted Y-type ferrite was also obtained up to $x = 0.5$. The Y-type phase is more unstable than the W-type phase with respect to this substitution rate.

Key words: W-type ferrite, Y-type ferrite, (ZnTi) substitution, solid state reaction, X-ray diffraction, Curie temperature, spontaneous magnetization, cation distribution

1. Introduction

The hexagonal ferrites have been investigated for electronic devices at microwave frequencies since their discovery in 1950s [1]. Their availability at high frequencies is caused by the large magnetic anisotropy constants and the preference to several magnetized directions, parallel or perpendicular to the hexagonal *c*-axis. Most of ferrites also have low eddy current loss at high frequency and corrosive resistance because they are oxides.

The crystal structure of hexagonal ferrites is based upon the close-packed structure of large oxygen anions and barium cations. The small transition metal cations (Fe^{3+} and Me^{2+}) are located between the larger ions. The structures of hexagonal ferrites can be represented by the stacking combinations along their hexagonal *c*-axis of R, S, and T blocks [2]. The chemical formulae for these blocks are as follows: R = $(BaFe_6O_{11})^{2-}$, S = $Me_2Fe_4O_8$ / $(Fe_6O_8)^{2+}$, T = $Ba_2Fe_8O_{14}$. The composition of the S block corresponds with the two formula units of the spinel ferrite. The major hexagonal ferrites are described by the following symbols: RSR^*S^* for M-type ($BaFe_{12}O_{19}$), $(RSR^*S^*S^*)_3$ for X-type ($Ba_2Me_2Fe_{28}O_{46}$), $RSSR^*S^*S^*$ for W-type ($BaMe_2Fe_{16}O_{27}$), $(TS)_3$ for Y-type ($Ba_2Me_2Fe_{12}O_{22}$), $RSTSR^*S^*T^*S^*$ for Z-type ($Ba_3Me_2Fe_{24}O_{41}$), and $(RSTSR^*S^*)_3$ for U-type ($Ba_4Me_2Fe_{36}O_{60}$) [3, 4]. The superscript * denotes that the layer is turned for 180° around the *c*-axis.

M-type barium ferrite ($BaFe_{12}O_{19}$) is widely used for permanent magnets due to its large magneto-crystalline anisotropy [5]. In addition, many research groups have investigated barium ferrite as microwave absorbers [6-8] and magnetic recording media [9] by modifying its anisotropy. The control of its magnetic property is achieved by the replacement of Fe^{3+} ions by Al^{3+} [10-13], Cr^{3+} [13-15] ions or pairs of ($Me^{2+}Mt^{4+}$) ions such as ($Co^{2+}Ti^{4+}$) [16, 17], ($Zn^{2+}Ti^{4+}$) [18, 19], ($Mn^{2+}Ti^{4+}$) [6, 20], ($Ni^{2+}Sn^{4+}$) [21], ($Co^{2+}Sn^{4+}$) [22], ($Co^{2+}Zr^{4+}$) [23, 24], where the Me and Mt represent divalent and tetravalent cations, respectively. The substitution effect on anisotropy is so significant that even the hard magnetic property of $BaFe_{12}O_{19}$ was changed to soft magnetic by substitution of $(Co^{2+}Zn^{2+})Ti^{4+}$ for Fe^{3+} [25].

On the other hand, W-type and Y-type ferrites have different magnetic properties from those of M-type ferrite due to their different stacking structures. W-type ferrite can possess higher saturation magnetization than that of M-type ferrite [26]. Y-type ferrite has planar anisotropy [27], which gives hope for high-frequency application. Therefore, the control of the magnetic properties of W-type and Y-type ferrites has been an important issue.

To the best of our knowledge, however, there are few investigations on the substituted W-type and Y-type ferrite. Maeda *et al.* reported the preparation by a conventional ceramic technique, magnetic properties, and microwave absorption properties of the ($Mn^{2+}Sn^{4+}$) and ($Mn^{2+}Zr^{4+}$) substituted W-type ferrite [28]. Ul-ain *et al.* reported the synthesis by sol-gel method and catalytic activities of the ($Mn^{2+}Ti^{4+}$) substituted Y-type ferrite [29]. Also, substitution limits of $Me^{2+}Mt^{4+}$ for Fe^{3+} in W-type and Y-type structures are unclear in contrast with that in the M-type structure where complete substitution of $Co^{2+}Ti^{4+}$ for Fe^{3+} is possible to form $BaCo_6Ti_6O_{19}$ [30].

We report the synthesis of the ($Zn^{2+}Ti^{4+}$) substituted hexagonal ferrites, $BaZn_2(Zn_{0.5}Ti_{0.5})_xFe_{16-x}O_{27}$ (W-type) and $Ba_2Zn_2(Zn_{0.5}Ti_{0.5})_xFe_{12-x}O_{22}$ (Y-type), and the relation between their composition and magnetic properties in this paper. Here, we employed $Zn^{2+}Ti^{4+}$ cations for substitution because an increase of the magnetization was expected if nonmagnetic cations replaced Fe cations

in spin down sublattices as observed in substituted spinels [31].

2. Experimental procedure

The samples were prepared by solid-state reaction. We used $BaCO_3$, ZnO, TiO_2, and α-Fe_2O_3 as starting materials. They were mixed in the desired composition of Ba : Zn : $(Zn_{0.5}Ti_{0.5})$: Fe = 1 : 2 : x : (16-x) for the W-type ferrite and Ba : Zn : $(Zn_{0.5}Ti_{0.5})$: Fe = 2 : 2 : x : (12-x) for the Y-type ferrite with $0.0 \leq x \leq 2.0$ in a ball-milling pot for 24 h. The mixed powders were pressed into disks and then pre-sintered at 900°C in air for 5 h. The products were ground in a mortar and then pulverized for 10 min. at the rate of 1100 r.p.m. in a vario-planetary mill. The fine powders were pressed into disks again and then sintered at 1100-1350°C in air for 5 h. Finally, the products were ground into powders in a mortar.

The crystal structures were examined by powder X-ray diffraction (XRD) with Cu-Kα radiation. The magnetizations were measured with a vibrating sample magnetometer (VSM), and a superconducting quantum interference device magnetometer (SQUID).

3. Results and discussion

We identified the crystalline phases of the W-type composition samples with $0.0 \leq x \leq 2.0$ sintered at 1200-1350°C by XRD. Fig. 1 shows phase relationship between sintering temperature and substitution rate x. At $0.0 \leq x \leq 1.5$, the W-type phase formed in the samples sintered at 1250°C, provided that the W-type phase was the minority phase for the sample with x = 1.5. The samples with $0.0 \leq x \leq 1.5$ sintered at 1300°C and 1350°C consisted of the main W-type phase. On the other hand, at sintering temperature of 1350°C, the sample contained the M-type and spinel minority phases. Since this temperature is near to the melting point of the other barium-iron oxides (e. g. $Ba_2Fe_2O_5$; T_m = 1370°C [32]), the W-type phase is likely to decompose. These results show that the sintering temperature of 1300°C is the suitable condition for the synthesis of the substituted W-type ferrites.

Fig. 2 shows XRD patterns of W-type composition samples with Ba : Zn : $(Zn_{0.5}Ti_{0.5})$: Fe = 1 : 2 : x : (16-x) sintered at 1300°C. The samples had the W-type structure at $0.0 \leq x \leq 1.5$. At x = 1.5, there were some

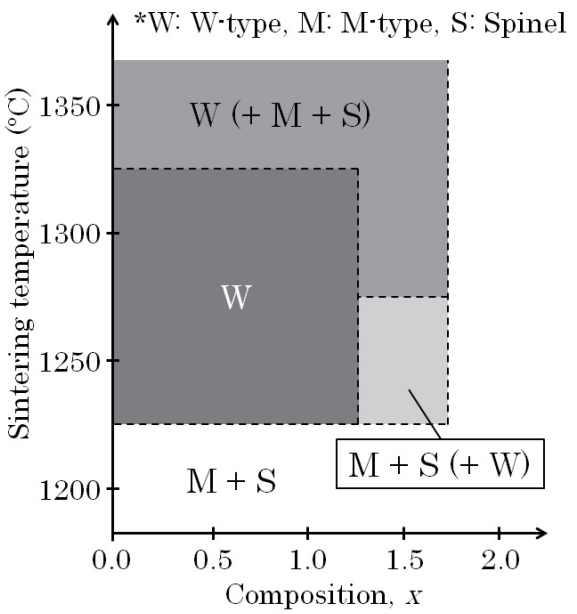

Fig. 1 Relationship between obtained crystalline phase and sintering temperature and substitution rate x for samples whose raw materials were mixed in composition of Ba : Zn : $(Zn_{0.5}Ti_{0.5})$: Fe = 1 : 2 : x : (16-x) with $0.0 \leq x \leq 2.0$. Phases in parentheses are minority phases.

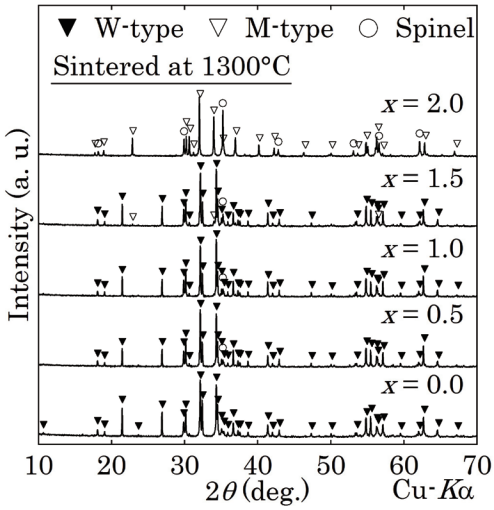

Fig. 2 XRD patterns for products sintered at 1300°C whose raw materials were mixed in composition of Ba : Zn : $(Zn_{0.5}Ti_{0.5})$: Fe = 1 : 2 : x : (16-x) with $0.0 \leq x \leq 2.0$.

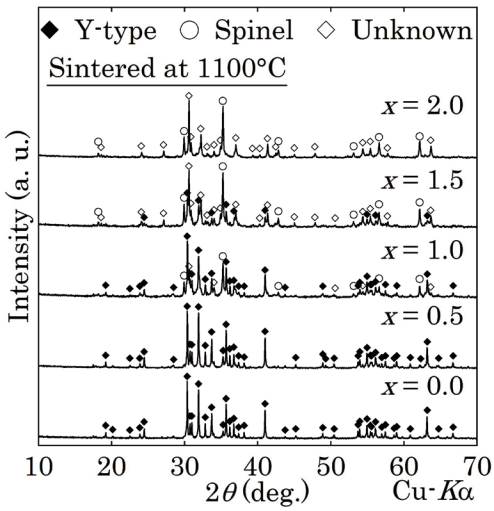

Fig. 3 XRD patterns for products sintered at 1100°C whose raw materials were mixed in composition of Ba : Zn : $(Zn_{0.5}Ti_{0.5})$: Fe = 2 : 2 : x : (12-x) with $0.0 \leq x \leq 2.0$.

weak diffraction peaks of the M-type and spinel ferrites. On the contrary, the peaks of the W-type phase disappeared in the pattern at $x = 2.0$. It should be noted that the first and second peaks of the W-type phase do not overlap those of the spinel and M-type phases as comparing the patterns between $x \leq 1.5$ and $x = 2.0$. Fig. 3 shows XRD patterns of Y-type composition samples with Ba : Zn : $(Zn_{0.5}Ti_{0.5})$: Fe = 2 : 2 : x : (12-x) sintered at 1100°C. We obtained the Y-type phase in the samples with $x = 0.0$ and 0.5. On the other hand, the diffraction peaks of the Y-type phase weakened at $x \geq 1.0$ and finally disappeared at $x = 2.0$. The phase identification was based on the diagrams of the BaO-ZnO-Fe_2O_3 [33], BaO-ZnO-TiO_2 [34] and BaO-Fe_2O_3-TiO_2 [35] systems, which showed no corresponding compounds except for the spinel and Y-type phases. The maximum substitution rate of (ZnTi)/(Fe+(ZnTi)) to form the single Y-type phase (0.5/12 ~ 4.2%) is smaller than that to form the single W-type phase (1.0/16 ~ 6.3%). Therefore, the Y-type phase is less stable than the W-type phase for $(Zn^{2+}Ti^{4+})$ substitution.

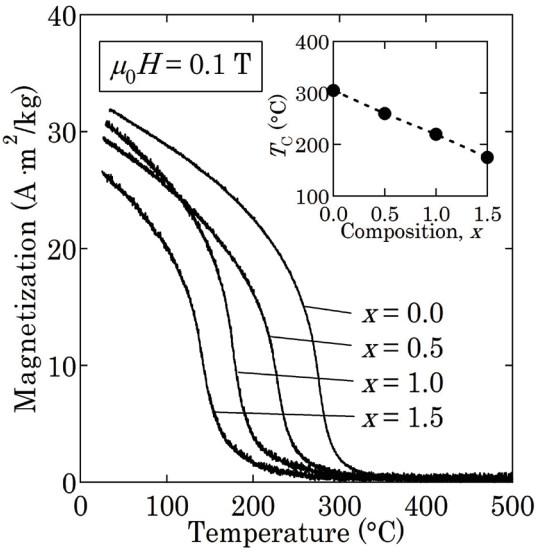

Fig. 4 Temperature dependences of magnetization at $\mu_0H = 0.1$ T for samples sintered at 1300°C whose raw materials were mixed in composition of $BaZn_2(Zn_{0.5}Ti_{0.5})_xFe_{16-x}O_{27}$ with $0.0 \leq x \leq 1.5$. Inset shows Curie temperatures T_C of those samples.

Fig. 4 shows temperature dependences of magnetization at $\mu_0H = 0.1$ T for W-type composition samples of $BaZn_2(Zn_{0.5}Ti_{0.5})_xFe_{16-x}O_{27}$ ($0.0 \leq x \leq 1.5$) sintered at 1300°C. Inset of Fig. 4 shows the Curie temperature T_C of the W-type phase as a function of the composition x, where T_C was estimated by linear extrapolation to zero-magnetization from the inflection point of the M-T curve. The Curie temperature T_C of the no-substitution sample ($x = 0.0$) was 305°C, which is in agreement with the previous report about $BaZn_2Fe_{16}O_{27}$ single crystals [36]. T_C linearly decreased with increasing x at $x \leq 1.5$, suggesting the exchange interactions between Fe^{3+} ions weakened. This fact implies that Zn^{2+} and Ti^{4+} cations successfully replaced Fe^{3+} cations in the W-type structure at $x \leq 1.5$.

Fig. 5 shows magnetization curves at $T = 5$ K (= –268°C) for W-type samples of $BaZn_2(Zn_{0.5}Ti_{0.5})_xFe_{16-x}O_{27}$ ($0.0 \leq x \leq 1.5$) sintered at 1300°C. The magnetization curve of the substituted samples at $x = 0.5$ was almost the same as that of the no-substitution sample ($x = 0.0$). Then, the magnetization decreased with increasing the substitution rate from $x = 0.5$ up to 1.5. This result is consistent with the fact that M-type ferrite showed similar Zn-Ti substitution dependence of spontaneous magnetization [37], where the magnetization began to

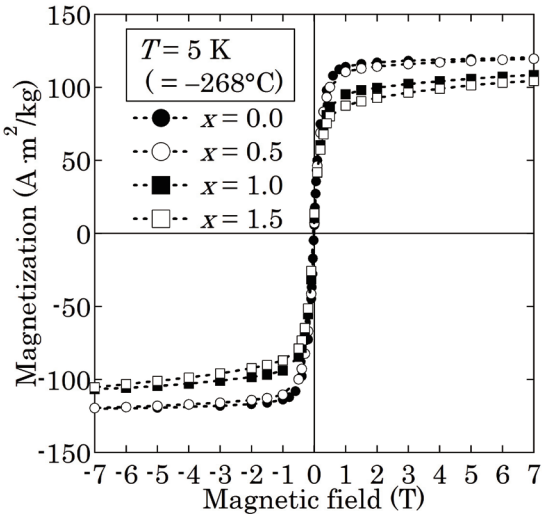

Fig. 5 Magnetization curves at $T = 5$ K (= –268°C) for samples sintered at 1300°C whose raw materials were mixed in composition of $BaZn_2(Zn_{0.5}Ti_{0.5})_xFe_{16-x}O_{27}$ with $0.0 \leq x \leq 1.5$.

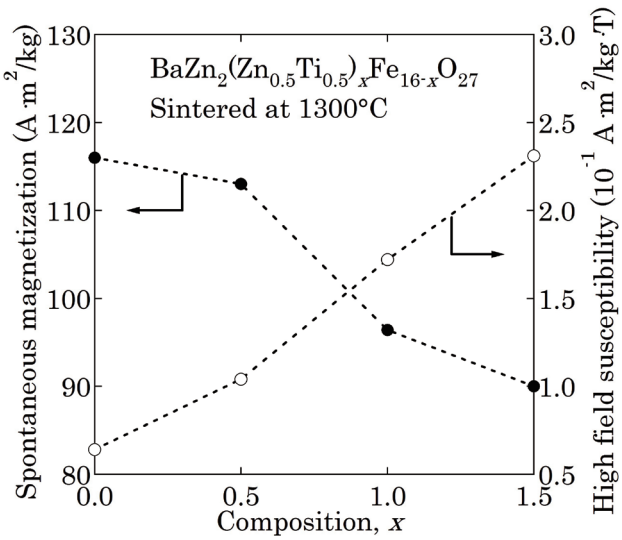

Fig. 6 Spontaneous magnetization and high field differential susceptibility for samples sintered at 1300°C whose raw materials were mixed in composition of $BaZn_2(Zn_{0.5}Ti_{0.5})_xFe_{16-x}O_{27}$ with $0.0 \leq x \leq 1.5$.

decrease above a certain Zn-Ti substitution rate.

Fig. 6 shows spontaneous magnetization σ_S and high field differential susceptibility χ_d as a function of the composition x. They were estimated by linear extrapolation of the magnetization curves from a high field region. The spontaneous magnetization σ_S slightly decreased from $x = 0.0$ to 0.5. In the range of $0.5 < x \leq 1.5$, the decrease of σ_S became more obvious. The substitution effect on σ_S seems to reflect Zn^{2+}-Ti^{4+} cation distribution in the W-type structure.

In order to discuss the relationship between the change in σ_S and the cation distribution in the W-type structure, we consider the spin configuration of the W-type structure. Table 1 shows the distribution of the transition metal sites and the expected directions of the magnetic moments in the R and S blocks of the W-type structure [38]. Fig. 7 also shows magnetic structure of W-type ferrite, corresponding to Table 1.

Concerning the cation distribution in the W-type structure, we assume that the Zn^{2+} ions prefer the 4*e* and 4f_{IV} sites and that Ti^{4+} ions prefer the 12*k* sites. In the case of the (ZnTi) substituted M-type ferrite [37], Zn^{2+} ions tend to enter the tetrahedral 4f_{IV} sites in the S block. Also, Ti^{4+} ions tend to enter the octahedral 4f_{VI} (the R block) sites and the 12*k* (the S and R blocks border) sites. In our W-type ferrite case, even with no substitution sample of $x = 0.0$, however, the positively charged part of two S blocks of $(Zn_2Fe_{10}O_{16})^{2+}$ and the negatively charged R block of $(BaFe_6O_{11})^{2-}$ are alternately stacked up as $SSRS^*S^*R^*$. The additional Zn^{2+} ions seem to occupy 4*e* and 4f_{IV} sites in the S blocks like the ZnTi-doped M-type ferrite. In order to keep the local electronic balance in the additional Zn^{2+} doped S blocks, Ti^{4+} ions may prefer the 12*k* sites to the 4f_{VI} sites because of the proximity to the Zn^{2+} sites in the S block.

We discuss the effect of the nonmagnetic ions upon the spontaneous magnetization σ_S depending on x. Between $x = 0.0$ and 0.5, the occupation of spin down (4*e* and 4f_{IV}) sites by Zn^{2+} ions can be cancelled out by the occupation of spin up (12*k*) sites by Ti^{4+} ions. Therefore, the decrease of σ_S is slight in this range. At $x > 0.5$, the obvious decrease of σ_S is possibly caused by the deviation from the collinear arrangement which can be dominant at high substitution rates of Zn^{2+} and Ti^{4+} ions [37]. To ascertain our estimation, further experimental investigations are needed to estimate the spin configuration and the cation distribution by Rietveld analysis on powder neutron diffraction [39] and X-ray absorption fine structure analysis [40].

The high field differential susceptibility χ_d for the substituted W-type ferrite increases with increasing x as shown in Fig. 6. It suggests that the magnetic structure of the substituted W-type ferrite becomes non-collinear especially at $x > 0.5$. It is consistent with the interpretation of the variation in σ_S discussed above.

Table 1 Coordination, number of ions, and spin orientation for various cation sublattices of W-type ferrite.

Block	Sublattice	Coordination	Number per block	Spin
S-S	6*g*	Octahedral	3	Up
S	4*e*	Tetrahedral	2	Down
S	4*f*	Octahedral	2	Up
S	4f_{IV}	Tetrahedral	2	Down
S-R	12*k*	Octahedral	6	Up
R	4f_{VI}	Octahedral	2	Down
R	2*d*	Trigonal -bipyramidal	1	Up

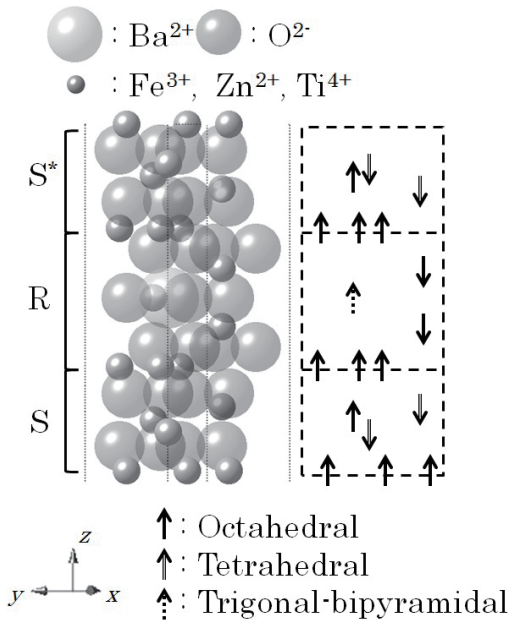

Fig. 7 Magnetic structure in half of unit cell (in formula unit) of W-type ferrite.

4. Conclusions

We report the synthesis condition and the magnetic properties of the $(Zn^{2+}Ti^{4+})$-substituted W-type and Y-type hexagonal ferrites that have hardly been investigated so far. The synthesis condition shows the substitution limits of $Zn^{2+}Ti^{4+}$ for Fe^{3+} in the W-type and Y-type ferrites, suggesting the stability of the W-type and Y-type structures.

The W-type composition samples sintered at 1300°C had the W-type structure in the region of $0.0 \leq x \leq 1.5$. The Curie temperature of the W-type phase decreased linearly with increasing x at $x \leq 1.5$. It suggests that the exchange interactions between the Fe^{3+} ions weakened due to the substitution of nonmagnetic Zn^{2+} and Ti^{4+} ions in the W-type structure. Spontaneous magnetization σ_S

at x = 0.5 was similar to that at x = 0.0. It reflects the equal distribution of nonmagnetic Zn^{2+} and Ti^{4+} ions to spin down sites and spin up sites, respectively. At $x > 0.5$, σ_s decreased clearly, which is possibly caused by the deviation from the collinear arrangement. It is consistent with the increase in the high field differential susceptibility χ_d with x.

The Y-type single phase was also obtained for the Y-type composition samples up to x = 0.5. The Y-type phase is more unstable than the W-type phase with respect to this substitution rate.

References

1) G. H. Jonker, H. P. J. Wijn and P. B. Braun: *Philips Tech. Rev.*, **18**, 145, (1956-1957).
2) J. Smit and H. P. Wijn: *Ferrites*, p. 150, 151, 180-189 (Philips Technical Library, London, 1959).
3) P. B. Braun: *Philips Res. Rep.*, **12**, 491-548 (1957).
4) T. Honda, Y. Hiraoka, Y. Wakabayashi and T. Kimura: *J. Phys. Soc. Jpn.*, **82**, 025003 (2013).
5) U. Ozgur, Y. Alivov and H. Morkoc: *J. Mater. Sci: Mater. Electron*, **20**, 789-834 (2009).
6) S. Sugimoto, K. Okayama, S. Kondo, H. Ota, M. Kimura, Y. Yoshida, H. Nakamura, D. Book, T. Kagotani and M. Homma: *Mater. Trans. JIM*, **39**, 1080-1083 (1998).
7) S. Sugimoto, S. Kondo, K. Okayama, H. Nakamura, D. Book, T. Kagotani and M. Homma: *IEEE Trans. Magn.*, **35**, 3154-3156 (1999).
8) K. Haga, S. Sugimoto, T. Kagotani and K. Inomata: *Mater. Trans.*, **45**, 2606-2609 (2004).
9) D. H. Han and Z. Yang: *IEEE Trans. Magn.*, **31**, 2351-2354 (1995).
10) A. V. Trukhanov, N. T. Dang, S. V. Trukhanov, S. H. Jabarov, I. S. Kazakevich, A. I. Mammadov, R. Z. Mekhdiyeva, V. A. Turchenko, and R. E. Huseynov: *Phys. Solid State*, **58**, 992–996 (2016).
11) C. J. Li, B. N. Huang and J. N. Wang: *J. Mater. Sci.*, **48**, 1702-1710 (2013).
12) S. M. El-Sayed, T. M. Meaz, M. A. Amer and H. A. El Shersaby: *Physica B*, **426**, 137-143 (2013).
13) J. Qiu, M. Gu and H. Shen: *J. Magn. Magn. Mat.*, **295**, 263-268 (2005).
14) J. Qiu, Y. Wang and M. Gu: *Mater. Lett.*, **60**, 2728-2732 (2006).
15) T. M. Meaz and C. B. Koch: *Hyperf. Interact*, **166**, 455-463 (2005).
16) A. M. Alsmadi, I. Bsoul, S. H. Mahmood, G. Alnawashi and K. Prokes: *J. Appl. Phys.*, **114**, 243910 (2013).
17) Y. Guan, Y. Lin, L. Zou, Q. Miao, M. Zeng, Z. Liu, X. Gao and J. Liu: *AIP Advances.*, **3**, 122115 (2013).
18) J. Li, H. Zhang, Y. Liu, Q. Li, G. Ma and H. Yang: *J. Mater. Electron,* **26**, 1060-1065 (2015).
19) Z. Yang, C. S. Wang, X. H. Li and H. X. Zeng: *Mater. Sci. Eng.*, **B90**, 142–145 (2002).
20) Y. S. Hong, C. M. Ho, H. Y. Hsu and C. T. Liu: *J. Magn. Magn. Mat.*, **279**, 401-410 (2004).
21) A. Gonzalez-Angelesa, G. Mendoza-Suareza, A. Gruskova, I. Toth, V. Jancarik, M. Papanova and J. I. Escalante-Garcia: *J. Magn. Magn. Mat.*, **270**, 77-83 (2004).
22) X. Gao, Y. Du, X. Liu, P. Xu and X. Han: *Mater. Res. Bull.*, **46**, 643-648 (2011).
23) R. K. Mudsainiyan, S. K. Chawla, S. S. Meena, N. Sharma, R. Singh and A. Das: *Ceram. Int.*, **40**, 16617-16626 (2014).
24) J. Zhou, H. Ma, M. Zhong, G. Xu, Z. Yue and Z. He: *J. Magn. Magn. Mat.*, **305**, 467-469 (2006).
25) K. Miyata, K. Kamishima, K. Kakizaki and N. Hiratsuka: *J. Magn. Soc. Jpn.*, **30**, 383-386 (2006) [in Japanese].
26) S. Chikazumi: Physics of Ferromagnetism, p. 213 (Oxford University Press, Oxford, 2009).
27) Ibid. 26, p. 282.
28) Y. Maeda, T. Kagotani, H. Nakamura, D. Book, S. Sugimoto and M. Homma: *J. Magn. Soc. Jpn.*, **24**, 895-898 (2000) [in Japanese].
29) B. Ul-ain, S. Ahmed, M. Anis ur Rehman, Y. Huang and C. A. Randall: *New J. Chem.*, **37**, 2768-2777 (2013).
30) A. Labarta, X. Batlle, B. Martínez, and X. Obradors: *Phys. Rev. B*, **46**, 8994-9001 (1992).
31) Ibid. 26, p. 204.
32) Y. Goto and T. Takada: *J. Am. Ceram. Soc.*, **43**, 150-153 (1960).
33) C. Slokar and E. Lucchini: *J. Magn. Magn. Mat.*, **8**, 232-236 (1978).
34) Phase Equilibria Diagrams, The American Ceramic Society and the National Institute of Standards and Technology, Figure Number 10032.
35) T. Siegrist and T. A. Vanderah: *Eur. J. Inorg. Chem.*, 1483-1501 (2003).
36) R. O. Savage and A. Tauber: *J. Am. Ceram. Soc.*, **47**, 13 (1964).
37) P. Wartewig, M. K. Krause, P. Esquinazi, S. Rosler and R. Sonntag: *J. Magn. Magn. Mat.*, **192**, 83-99 (1999).
38) G. Albanese and M. Carbucicchio: *Appl. Phys.*, **11**, 81-88 (1976).
39) T. Tachibana, T. Nakagawa, Y. Takada, K. Izumi, T. A. Yamamoto, T. Shimada and S. Kawano: *J. Magn. Magn. Mat.*, **262**, 248-257 (2003).
40) T. Nakagawa, M. Yuya, T. Tachibana, Y. Takada, H. Nitani, S. Emura, T. A. Yamamoto: *J. Magn. Magn. Mat.*, **288**, 366-373 (2005).

Received Jul. 20, 2017; Revised Sept. 3, 2017; Accepted Sept. 19, 2017

J. Magn. Soc. Jpn., **41**, 132-139 (2017)

<Paper>

Low permeability composite magnetic core transformer with high coupling coefficient and its application to PFM controlled quasi-resonant mode flyback-type DC-DC converter

K. Sato[*,**], T. Sato[**], M. Sonehara[**], and H. Takeuchi[*]

[*]Nagano Prefecture General Industrial Technology Center, *1-3-1 Osachi-katamacho, Okaya, Nagano 394-0084, Japan*

[**] Faculty of Engineering, Shinshu Univ., *4-17-1 Wakasato, Nagano, Nagano 380-0928, Japan*

We describe a low permeability composite magnetic core transformer with a high coupling coefficient and its application to a PFM controlled quasi-resonant mode flyback-type DC-DC converter. To increase the coupling coefficient between primary and secondary windings embedded in a carbonyl-iron powder/epoxy composite magnetic core with a relative permeability of 6, three types of winding layouts were investigated by using a 2D-FEA numerical simulation and the characteristics were confirmed experimentally. The primary and secondary windings that were laid out adjacent to each other were the best choice as it had the highest coupling coefficient at over 0.99. By applying the composite magnetic core transformer with this coupling coefficient to a 48 V input/12 V output PFM controlled quasi-resonant mode flyback-type DC-DC converter, the maximum efficiency was 92.5% at an output power of around 28 W, and an efficiency of 90.0% was obtained at an output power of 60 W.

Key words: low permeability magnetic core, carbonyl-iron powder/epoxy composite magnetic core transformer, winding layout, coupling coefficient, DC-DC converter, efficiency

1. Introduction

Recently, SiC/GaN power devices have been applied to switching power converters. It is because they make possible to have good advantages such as lower ON resistance, higher speed switching operation and higher temperature operation than the Si-based power devices [1), 2)]. By using the novel power devices, it is possible not only to increase the power conversion efficiency of the converter but also to downsize the magnetic devices used in the switching power converters since the switching frequency can be increased to MHz band or tens of MHz. However, it is considered difficult to use the magnetic devices consisting of dust core or Mn-Zn ferrite core for such the very high frequency switching power converter. M. Harrison[3)] stated that the possible magnetic core for MHz band or beyond 10 MHz power conversion would be Ni-Zn ferrite core only.

The authors are developing a novel magnetic core as a candidate substitute for the Ni-Zn ferrite core, for example, the carbonyl-iron powder/epoxy composite magnetic core was developed[4)] and was applied to switching power converters[5),6)]. In order to increase the volume resistivity of the composite magnetic core body, the surface-oxidation for the carbonyl-iron powder was very effective[4)]. Though the surface-oxidized carbonyl-iron powder/epoxy composite magnetic core had a low relative permeability of about 6, the magnetic loss was very small up to 10 MHz in frequency. By applying the composite magnetic core inductor to a 1 MHz switching buck-type DC-DC converter using GaN power device, a maximum power conversion efficiency of 93% was obtained[5)]. It was also reported that a composite magnetic core transformer with copper-clad polyimide tape windings embedded in the composite magnetic core could realize a coupling coefficient k > 0.99 even when using such the low permeability composite magnetic core[6)]. Furthermore, by applying the composite magnetic core transformer to a PWM (Pulse Width Modulation) controlled flyback-type DC-DC converter, the maximum power conversion efficiency was 91% at 400 kHz switching and 85% at 1 MHz switching[6)].

In general, the low permeability magnetic material is not suitable for transformer core because of large leakage inductance owing to the low coupling coefficient between the windings. This study was done to develop the composite magnetic core transformer with high coupling coefficient and to apply it to a PFM (Pulse Frequency Modulation) controlled quasi-resonant mode flyback-type DC-DC converter[7)].

This paper describes an investigation on the design of low permeability composite magnetic core transformer with high coupling coefficient on the bases of the two-dimensional finite element analysis (2D-FEA) numerical simulation and experiments. In addition, a PFM controlled quasi-resonant mode flyback-type DC-DC converter using the fabricated composite magnetic core transformer is also shown.

2. Surface-oxidized carbonyl-iron powder/epoxy composite magnetic core transformer

2.1 Properties of surface-oxidized carbonyl-iron powder/epoxy composite magnetic core

As the soft magnetic metal powder for the composite magnetic core, non-reduction carbonyl-iron powder with a mean diameter of 1.6 μm was used. In order to prevent the electrical contact between the adjacent powders in the composite magnetic core and to

suppress the over-lapped eddy current loss, high resistive oxidized layer of several tens of nm was introduced on the surface of the powders by thermal oxidation in air at 200 degrees-C for 6h[4]. The composite magnetic core was fabricated by the casting and post-curing using the composite slurry with the surface-oxidized carbonyl-iron powder and epoxy precursor solution. Since the nonmagnetic epoxy resin between the magnetic particles behaves as a magnetic gap, the composite magnetic core is hard to be magnetically saturated due to its low permeability and has superior superimposed DC current characteristics when using the magnetic devices, so that the transformer core can be gapless.

Fig. 1 shows the static magnetization curve of the surface-oxidized carbonyl-iron powder/epoxy composite magnetic core measured by using a VSM (Riken Denshi Co., Ltd.; BHV-55). The saturation magnetization was about 1 T. Though the composite magnetic core had nonmagnetic epoxy resin, it exhibited a high saturation magnetization around 1 T, so it was considered that the energy density could be increased and the transformer core could be downsized.

Fig. 2 shows the frequency dependence of the relative complex permeability of the surface-oxidized carbonyl-iron powder/epoxy composite magnetic core measured by using an impedance/material analyzer

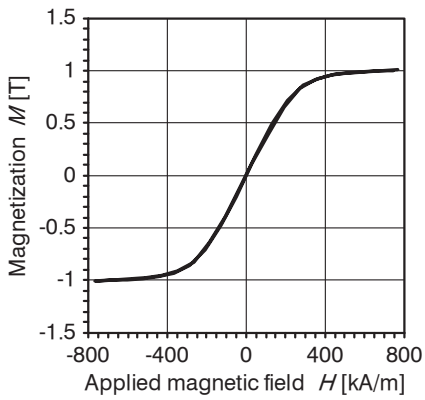

Fig. 1 Static magnetization curve of surface-oxidized carbonyl-iron powder/epoxy composite magnetic core.

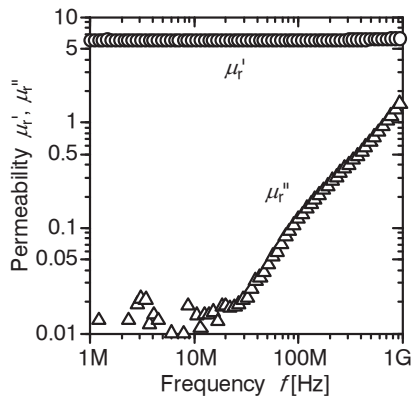

Fig. 2 Complex relative permeability of surface- oxidized carbonyl-iron powder/epoxy composite magnetic core.

(Agilent; 4291B) and a coaxial waveguide. The real part of the complex relative permeability μ_r' was low as about 6, but the imaginary part μ_r" was as small as 10^{-2} order at 10 MHz or less. Although not measured below 1 MHz in frequency, the relative permeability μ_r' of about 6 was considered to be constant at hundreds kHz band and the magnetic loss μ_r" was considered to be small enough at same hundreds kHz band.

The volume resistivity of the surface-oxidized carbonyl-iron powder/epoxy composite magnetic core was about 100 Ω•m[4], which was 100 times higher than that of Mn-Zn ferrite core. Therefore, it was considered that the eddy current loss of the transformer core could be significantly suppressed at least up to 10 MHz.

2.2 Transformer structure

The output voltage of the quasi-resonant mode flyback-type DC-DC converter is controlled by changing both the on pulse width and the switching frequency according to the output current[7]. As the output power becomes larger, the on pulse width expands and the switching frequency decreases. Also, the soft switching operation can be realized by using the resonance of the drain-source voltage of the MOSFET due to the inductance of the transformer primary winding and the capacitor connected in parallel to the MOSFET. Therefore, in order to increase the switching frequency, it is necessary to reduce the inductance of the primary winding. Since the composite magnetic core under investigation has a high saturation magnetization and the operating range ΔB of the transformer can be enlarged, even when the switching frequency decreases under heavy load, the magnetic saturation occurs hardly, which is due to the low inductance (low permeability composite magnetic core).

Fig. 3 shows the composite magnetic core transformer structure under investigation in this paper. The transformer winding was embedded in the composite magnetic core with a 30 mm-square size and

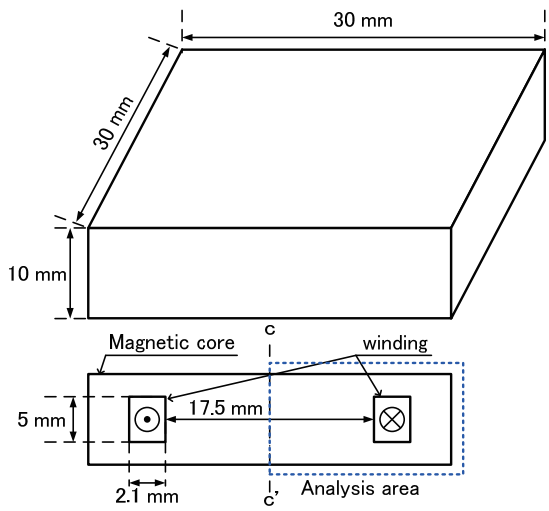

Fig. 3 Composite magnetic core transformer with embedded windings.

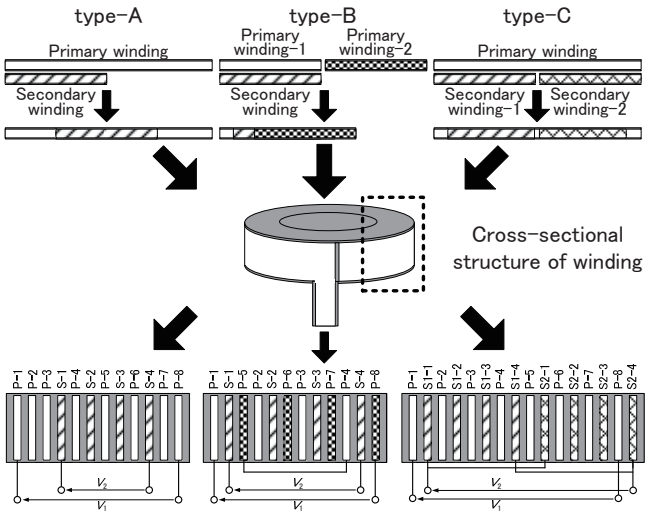

Fig. 4 Three types of winding layouts for composite magnetic core transformers with embedded windings.

10 mm in thickness. A copper-clad polyimide tape having a 70 μm thick, 5 mm wide copper conductor line formed on a 100 μm thick, 5.2 mm wide polyimide tape was used as the primary and secondary winding.

In this paper, inductance of the primary winding was designed so that the switching frequency was about 500 kHz when the converter output power of 60 W[8]. For a reason of the fabrication process of the tape wound coil, the number of turns was determined to be an even number, the primary winding turn was 8, and the secondary winding turn was 4. Since the composite magnetic core had a low relative permeability, winding layout becomes more important than when using other magnetic core materials having a high relative permeability. In general, when the primary and secondary winding were wound in an interleaved structure, the coupling coefficient between the windings could be increased[9)-11)]. It was easy to wind in an interleaved structure when the number of turns of primary winding and that of secondary windings were equal. However, since the number of turns of primary and secondary winding of the transformer discussed in this paper was different, three types of transformers having different winding layout as shown in Fig. 4 were studied. In the cross-sectional view of windings in the lower figure of Fig. 4, "P-1" to "P-8" means from first turn to eighth turn of the primary winding, respectively. Similarly, "S-1" to "S-4" means from first turn to fourth turn of the secondary winding, respectively.

Type-A transformer consisted of one primary winding and one secondary winding. The secondary winding was concentratedly laid out near the center of the primary winding when looking at the cross-sectional structure of the windings. Therefore, the innermost conductors of the primary winding and the secondary winding were not adjacent to each other.

Type-B transformer consisted of two primary windings and one secondary winding. The secondary winding was sandwiched between two primary windings and wound four turns. In order to make the primary winding eight turns, the winding end of one of the two primary windings and the winding start of the other were connected in series outside the magnetic core. Hence, the innermost conductors of the primary winding and the secondary winding were adjacent to each other, and the secondary winding were distributed and evenly laid out between the primary winding when looking at the cross-sectional structure of the windings.

Type-C transformer consisted of one primary winding and two secondary windings. After the first secondary winding was wound four turns with the primary winding, the second secondary winding was wound continuously four turns with the primary winding. In order to make the secondary winding four turns, two secondary windings were connected in parallel outside the magnetic core. As shown in Fig. 4, the innermost conductors of the primary winding and the secondary winding were adjacent to each other and the secondary winding of type-C were alternately and evenly laid out between the primary winding when looking at the cross-sectional structure of the windings. The inductance and the resistance of the two secondary windings were different because the lengths and inner diameters were different. Hence, it was considered that an imbalance in the current flowing of the two secondary windings may occurs. The following 2D-FEA numerical simulation and experiments took this behavior into account.

2.3 Fabrication procedure of composite magnetic core transformer

The fabrication procedure of the composite magnetic core transformer is as follows. An air-core winding having an inner diameter of 17.5 mm was fabricated. Air-core windings were covered with polyimide tape to prevent contact between the winding and the composite magnetic core material. The composite slurry was prepared by mixing surface-oxidized carbonyl-iron powder and two component epoxy precursor solution. The slurry was filled in a mold in which the winding was arranged and then cured at 120 degrees-C for 5 h. Thereafter, the size of the composite magnetic core was adjusted by polishing. As the lead wire from the winding inside the composite magnetic core, the same copper-clad polyimide tape was used.

3. Operation analysis for composite magnetic core transformer

3.1 Analysis model and conditions

In order to clarify the operation characteristics of the three types of transformers, 2D-FEA numerical simulation (Ansys; Maxwell) was introduced. As shown in Fig. 3, the analytical region was set to be the right half of the transformer cross section because of the symmetry of the device structure. The analytical model for deriving various parameters was a model rotated

Table 1 Parameters for 2D-FEA numerical simulation for three types of composite magnetic core transformers.

Material	Constant
Composite magnetic core	Permeability: $\mu_r' = 6$ (const.) Loss tangent: $\tan\delta = 0.002$ (const.) Conductivity: 0.01 S/m (100 Ω•m)
Conductor line (Copper)	Conductivity: 5.8×10^7 S/m Thickness: 70 μm, Width: 5 mm
Insulator layer (Polyimide)	Conductivity: 0 S/m Thickness: 100 μm, Width: 5.2 mm

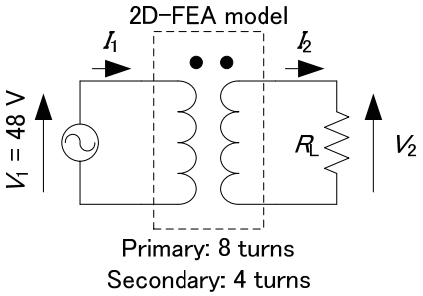

Fig. 5 Relationship between 2D-FEA numerical simulation for composite magnetic core transformer and equivalent circuit.

one time around c-c' by post processing of the simulator. For this reason, the transformer core of the analytical model had a cylindrical shape with a diameter of 30 mm and a thickness of 10 mm, and the outer shape was different from the fabricated transformer. However, it was considered that there was little influence on the analysis result since the magnetic circuit of the transformer core had almost the same structure. The 2D-FEA could not accurately simulate the three-dimensional structure of the transformer including the influence of the lead wire etc. Therefore, quantitative consideration was difficult. However, it was considered sufficient to consider the relationship between the winding layout of the transformer and its operating characteristics under the same magnetic circuit structural condition.

Table 1 shows the properties used for analysis. The copper loss of the winding was calculated with taking the losses due to the skin effect and the proximity effect into account. The magnetic properties of the composite magnetic core were regarded as linear, and the magnetic hysteresis was not considered. The core loss was calculated from the imaginary part of the complex permeability shown in Fig. 2 and set as the loss tangent $\tan\delta$ ($=\mu_r''/\mu_r'$) in the 2D-FEA numerical simulation. Since the measurement variation of the imaginary part of complex permeability in the low frequency below 10 MHz was large, the value of $\tan\delta$ at 10 MHz was also used for the analysis below 10 MHz. Analysis was carried out under the constant voltage source excitation by using "Maxwell Circuit Editor" function capable of coupled analysis of FEA and the circuit simulation, the circuit diagram as shown in Fig. 5 was introduced, and

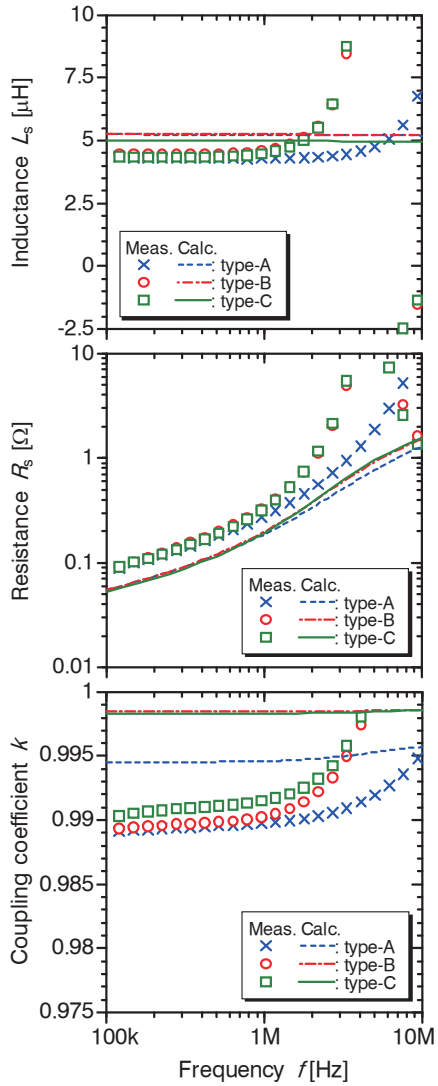

Fig. 6 Frequency characteristics of three types of transformers.

the operation characteristics of the transformers were simulated. In Fig. 5, a sinusoidal voltage source was connected to the primary side of the transformer, and a resistive load was connected to the secondary side. The input voltage V_1 was set to 48 V_{rms}.

Since the measured value of the relative permeability in Fig. 2 was a small signal characteristic and $\tan\delta$ was regarded as constant value, the calculated power loss may be estimated to be smaller than the actual power loss. However, for the purpose of comparing the differences in characteristics due to the winding layout, the essential problem was considered to be small.

3.2 Electrical characteristics

Fig. 6 shows the equivalent series inductance, equivalent series resistance and coupling coefficient of the primary side of the transformer at the time of no-load. In Fig. 6, the plots are measured values by using an impedance/gain-phase analyzer (Agilent; 4194A) and the solid lines are calculated ones. The

Table 2 Measured and calculated DC resistance of each winding of transformers.

		Measured	Calculated
type-A	Primary	26.6 mΩ	24.0 mΩ
	Secondary	14.5 mΩ	12.1 mΩ
type-B	Primary	28.8 mΩ	24.1 mΩ
	Secondary	14.8 mΩ	12.0 mΩ
type-C	Primary	27.4 mΩ	24.7 mΩ
	Secondary	7.2 mΩ	6.3 mΩ

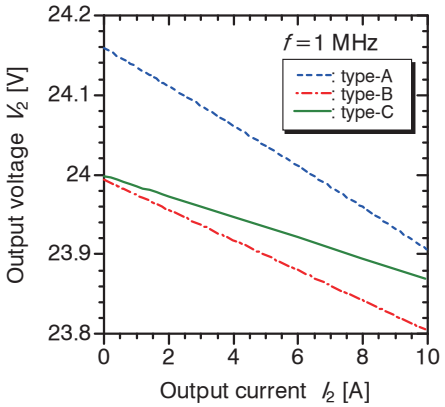

Fig. 7 Analysis results of load current dependence of output voltage for three types of transformers.

coupling coefficient was obtained by the secondary side open/short circuit method.

As shown in Fig.6, the equivalent series inductance of the fabricated transformer was about 4.6 μH regardless of the winding layout. The self-resonance frequency of type-B and type-C was lower than that of type-A because of the parasitic capacitance increase due to the winding layout[5].

Table 2 shows the measured and calculated DC resistance of each winding of the transformers. As shown in Table 2, the DC resistance of the primary windings was almost equal regardless of the winding layout. However, since two windings were connected in parallel, the DC resistance of the secondary winding of type-C was almost half.

Although there was the difference between the measured values and the calculated ones of each parameter, this was considered to be due to the positional deviation of the winding in the thickness direction of the magnetic core[5] and the influence of the parasitic parameters of the lead wire from the winding inside the composite magnetic core not considered in the analytical model. Also, since 2D-FEA was only magnetic field analysis, the influence of self-resonance did not appear in the calculation results. However, the tendency of the electrical characteristics of the three transformers generally agrees with the measured values and the calculated ones, it was considered that it was possible to compare the difference in characteristics due to the winding layout.

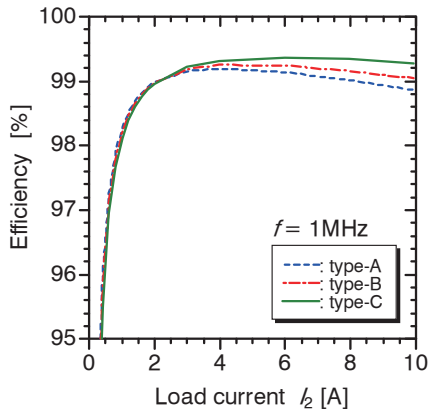

Fig. 8 Analysis results of load current dependence of efficiency for three types of transformers.

3.3 Load current dependences of transformer

Fig. 7 shows the calculated load current dependence of the output voltage V_2 of transformer. As shown in Fig. 7, the output voltage V_2 of type-A exceeded 24 V in the no-load and light load, which was higher than the value calculated from the turn ratio of 8:4. It was considered to be due to the low relative permeability of the composite magnetic core. Since the relative permeability was low, the main magnetic flux was considered not only to have the component in the composite magnetic core body but also to include the leakage component in the region near to the primary winding. As a result, the effective inner diameter of the secondary winding was considered to be enlarged and the inductance also increased. This was equivalent to the increase of the number of turns of the secondary winding. Hence, it was considered that the output voltage became higher than the value calculated from the turn ratio of 8:4. This operation suggests that the operating point of the transformer may unintentionally change from the operating point designed based on the specifications of the converter. On the other hand, in type-B and type-C, since the innermost conductors of the primary winding and the secondary winding were adjacent to each other and there was almost no difference in inner diameter, the output voltage was almost equal to the calculated value from the turn ratio of 8:4.

The output voltage of type-A transformer decreased more than the other two types of transformers. It was considered because type-A had lower coupling coefficient between primary and secondary winding than the other two types of transformers, and its leakage inductance was larger than the other two transformers.

3.4 Power efficiency and loss

Fig. 8 shows the calculated power efficiency of the transformer at 1 MHz. The maximum efficiency of 99% or more in any transformer was obtained. Since the loss due to the excitation current was mainly at no-load and light load, the type-A transformer with the lowest

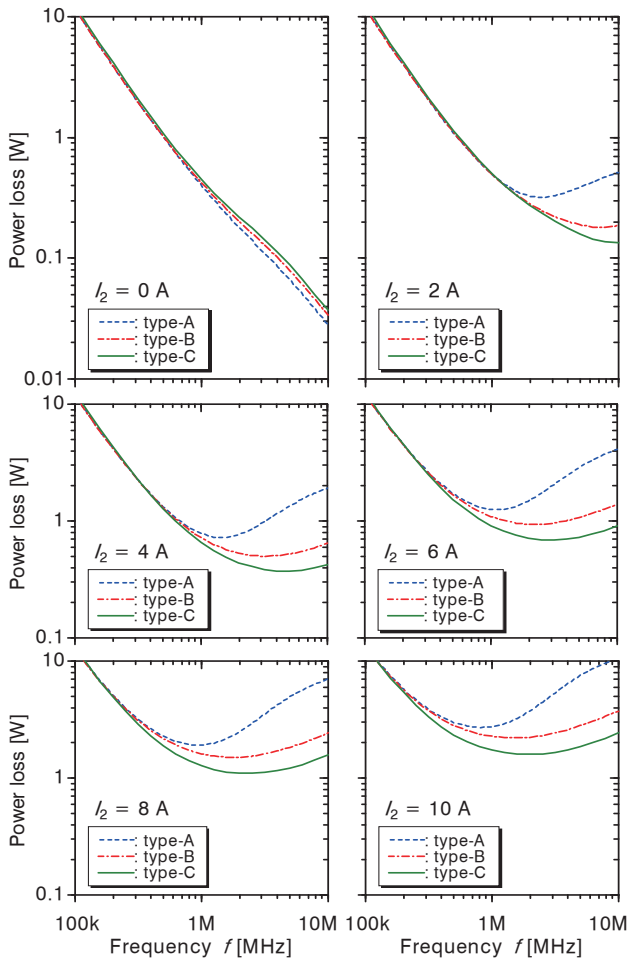

Fig. 9 Analysis results of frequency dependence of power loss for three types of transformers.

equivalent series resistance of primary winding at 1 MHz had the highest power efficiency. On the other hand, at heavy load, type-C with lowest secondary winding resistance and highest coupling coefficient between windings had the highest power efficiency.

Fig. 9 shows the calculated values of the frequency dependence of the power loss of the transformer. The frequency at the minimum power loss varied with the load current value, and the composite magnetic core transformers under investigation in this study exhibited the minimum power loss obtained at 500 kHz to 2 MHz according to the load current intending for the PFM controlled quasi-resonant type flyback converter in this study. The power loss in the low frequency increased because the winding loss increased and the input power factor decreased, which was considered to be owing to the low inductance and the increase of excitation current with lowering frequency. On the other hand, it was considered that the power loss increased in the high frequency due to the skin effect and proximity effect of the windings.

With increasing load current I_2, the frequency at the minimum power loss shifted to the low frequency side in any transformer. In the quasi-resonant mode flyback-type DC-DC converter, since the switching frequency decreases with increasing load current, there is a possibility that high efficiency can be maintained in the wide load condition when the composite magnetic core transformer is applied to such converter.

3.5 Magnetic flux density distribution in transformer

Fig. 10 shows the calculated magnetic flux density distribution of the three types of transformers when the frequency of 1 MHz and load current of 10 A. In Fig. 10, the in-phase flux component with the exciting current and 90-degrees phase-lag component are shown, where the stored energy in the transformer corresponds to the in-phase flux component and the energy loss corresponds to the 90-degrees phase-lag component. Since the magnetic loss due to tanδ (=μ_r"/ μ_r') of the composite magnetic core was considered to be small enough at 1 MHz, the energy loss was considered to be mainly due to the windings.

From upper figure in Fig. 10, it was found that the in-phase magnetic flux density with the exciting current occurred mainly inside the winding and its spatial distribution was almost same in three types of winding layouts. On the other hand, as shown in the lower figure in Fig. 10, 90-degrees phase-lag magnetic flux density component shows a difference depending on the winding layout. In the type-A, 90-degrees phase-lag magnetic flux density distribution was generated between the conductors where the primary winding and the secondary winding were adjacent to each other. In particular, the magnetic flux was also distributed in the composite magnetic core at the beginning and the end of the secondary winding. Also in type-B, 90-degrees phase-lag magnetic flux was generated between the conductors where the primary winding and the secondary winding were adjacent to each other, but no 90-degrees phase-lag magnetic flux was generated in the composite magnetic core. Type-C had little 90-degrees phase-lag magnetic flux in the composite magnetic core and the 90-degrees phase-lag magnetic flux density between windings was smaller than type-B. It was considered that the 90-degrees phase-lag magnetic flux density component was due to the energy loss owing to the difference between the primary magnetomotive force and the secondary magnetomotive force. It was suggested that offsetting both the magnetomotive forces was incomplete in type-A. Furthermore, the leakage magnetic flux due to the offset magnetomotive force was considered to be a cause of an increase in eddy current loss in the winding. Therefore, it was inferred that type-A had larger winding loss at the large offset magnetomotive force when the heavy load, compared with the other two types of transformers. It was considered that the difference between the losses of type-B and type-C was not only due to the winding resistance of the secondary winding but also due to the influence of the eddy current loss caused by the leakage magnetic flux.

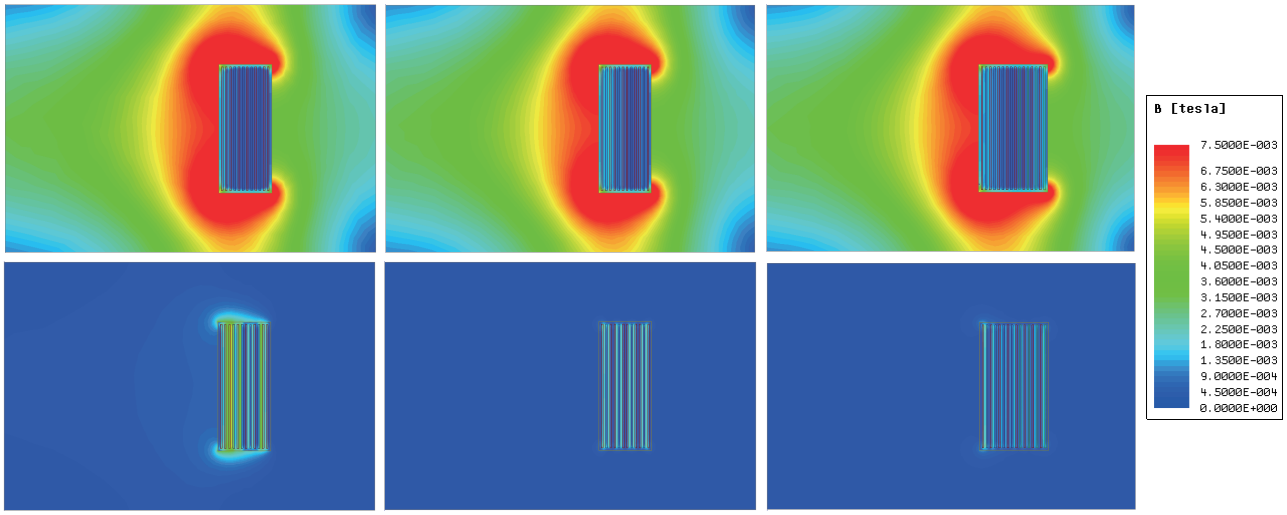

type-A type-B type-C

Fig. 10 Magnetic flux density distributions of three types of transformers. Upper figure represents in-phase flux component with exciting current, and lower figure shows flux component with 90-degree phase-lag from exciting current when frequency was 1 MHz and load current was 10 A.

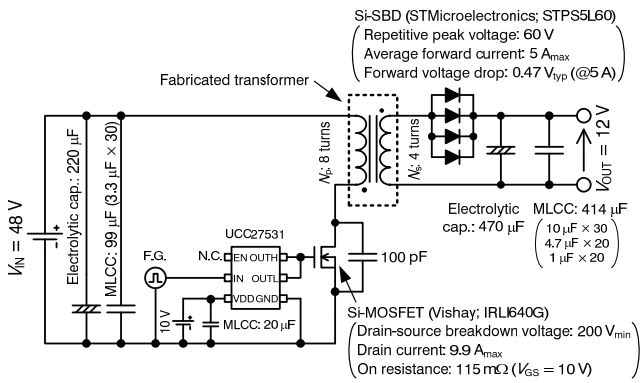

Fig. 11 Circuit diagram of PFM controlled quasi-resonant mode flyback-type DC-DC converter.

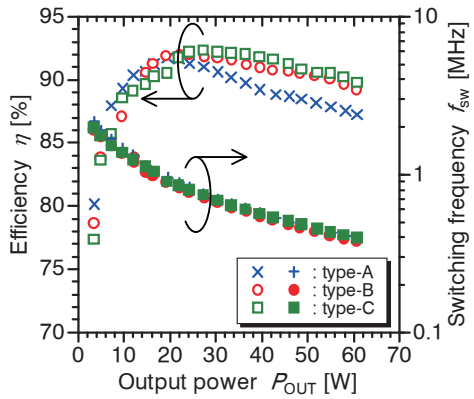

Fig. 12 Power conversion efficiency and switching frequency of converter using composite magnetic core transformers with different winding layouts.

4. Application to PFM controlled quasi-resonant mode flyback-type DC-DC converter

4.1 Evaluation circuit diagram and conditions

Since the PFM controlled quasi-resonant mode flyback-type DC-DC converter[7] used in this study operates under the critical current mode and soft switching operation, it is expected to realize both higher conversion efficiency and higher switching frequency.

Fig. 11 shows the circuit diagram of the PFM controlled quasi-resonant mode flyback-type DC-DC converter with the composite magnetic core transformer under investigation. While the drain-source voltage waveform of the MOSFET was being confirmed with the oscilloscope, the switching frequency and on-time ratio were adjusted by the function generator (YOKOGAWA; FG420) so that the output voltage was constant at 12 V even if the output current was changed.

4.2 Experimental results and discussion

Fig. 12 shows the measured power conversion efficiency and switching frequency of the converter using three types of composite magnetic core transformers. In this evaluation condition, the switching frequency varied from approximately 400 kHz to 2 MHz, which was roughly in agreement with the frequency band in which the power loss of the composite magnetic core transformer was small in the above-described operation analysis for the transformers. As shown in Fig. 12, when type-C was used, the maximum power conversion efficiency was 92.5% at an output power of around 28 W, and an efficiency of 90% was obtained at an output power of 60 W.

Power conversion efficiency at the light load was highest when type-A was used. However, with increasing the output power, the power conversion efficiency decreased significantly. Main reason of the efficiency decrease at large output power condition was considered to be owing to the increase of eddy current loss in the winding, where the leakage flux generated by the difference of the magnetomotive forces between

primary and secondary winding became large when heavy load condition. On the other hand, in type-B and type-C, the decrease in power conversion efficiency was small even if the output power increases. These trends were consistent with the results of power loss analysis for the transformers.

5. Conclusion

In general, the low permeability magnetic core is not suitable for transformer because of large leakage inductance owing to the low coupling coefficient between windings. Though the surface-oxidized carbonyl-iron powder/epoxy composite magnetic core has a low relative permeability of about 6, its magnetic loss was small below 10 MHz in frequency.

This study was done to develop the surface-oxidized carbonyl-iron powder/epoxy composite magnetic core transformer with high coupling coefficient and to apply it to the PFM controlled quasi-resonant mode flyback-type DC-DC converter. The obtained results are as follows.

(1) In order to obtain high coupling coefficient, the embedded winding structure was introduced to the composite magnetic core transformer design, and the three kinds of winding layouts were investigated on the bases of 2D-FEA numerical simulation and experiments. The adjacent layout of the primary and secondary winding was best choice for highest coupling coefficient over 0.99.

(2) The output voltage of the transformer, in which the innermost of the primary winding and the secondary winding were not adjacent to each other and had low coupling coefficient, was higher than the value calculated from the turn ratio at the no-load and light load. This operation suggests that the operating point of the transformer may unintentionally change from the operating point designed based on the specifications of the converter.

(3) The frequency at the minimum power loss shifted to the low frequency side with increasing load current in any transformer under investigation in this study, and the transformers exhibited the minimum power loss obtained at 500 kHz to 2 MHz according to the load current intending for the PFM controlled quasi-resonant type flyback converter in this study. Since the switching frequency of the converter decreases with increasing load current, there is a possibility that high efficiency can be maintained in the wide load condition when the composite magnetic core transformer is applied to such converter.

(4) Application of the fabricated composite magnetic core transformer with the best winding layout described in above (1) to the 48 V input/12 V output PFM controlled quasi-resonant mode flyback-type DC-DC converter exhibited a maximum power conversion efficiency of 92.5% at an output power of around 28 W, and 90% efficiency was obtained at an output power of 60 W. The obtained efficiency characteristics were consistent with the trend of power loss analysis for the composite magnetic core transformers.

Acknowledgements This study was supported in part by Grant-in-Aids for Japan Society for the Promotion of Science (15H02233), New Energy and Industrial Technology Development Organization (15101041-0), Japan, and Japan Science and Technology Agency (Nagano Satellite Cluster, Kyoto Super Cluster Program).

References

1) A. León-Masich, H. Valderrama-Blavi, J. M. Bosque-Moncusí, and L. Martínez-Salamero: *IET Power Electronics*, **8**, 6, pp.869-878 (2015).
2) H. Wang, A. M. H. Kwan, Q. Jiang, and K. J. Chen: *IEEE Trans. Electron Devices*, **62**, 4, pp.1143-1149 (2015).
3) M. Harrison: Plenary session, *IEEE Applied Power Electronics Conf. and Expo. (APEC) 2016*, Long Beach, CA, USA (2016).
4) K. Sugimura, Y. Miyajima, M. Sonehara, T. Sato, F. Hayashi, N. Zettsu, K. Teshima and M. Mizusaki: *AIP Advances*, **6**, 055932-1-8 (2016).
5) D. Shibamoto, A. Ueno, K. Sugimura, R. Hirayama, K. Sato, T. Sato, and M. Sonehara; *The Papers of Joint Technical Meeting on "Magnetics" and "Linear Drives"*, MAG-16-041/LD-16-033, pp.17-22 (2016) (in Japanese).
6) K. Sato, K. Sugimura, T. Sato, M. Sonehara, and H. Takeuchi; *T. Magn. Soc. Jpn. (Special Issues).*, **1**, pp.44-52 (2017) (in Japanese).
7) Y. Asako, H. Shiroyama, Y. Ishizuka, H. Matsuo; *IEICE Technical Report*, EE2007-64/CPM2007-149, pp.1-6 (2008) (in Japanese).
8) J. Togawa: Suicching-dengen no koiru/toransu sekkei (in Japanese), pp.201-209 (CQ shuppansha, Tokyo, 2012).
9) T. Sato, H. Yokoyama, K. Yamasawa, K. Toya, S. Kobayashi, T. Minamisawa; *T. IEE Japan*, **120-A**, 3, pp.266-271 (2000) (in Japanese).
10) Z. Ouyang, J. Zhang, W. G. Hurley; *IEEE Trans. Power Electronics*, **30**, 10, pp.5769-5775 (2015).
11) H. Tanaka, K. Nakamura, O. Ichinokura; *J. Magn. Soc. Jpn*, **40**, pp.35-38 (2016).

Received June 13, 2017; Revised July 10, 2017; Accepted July 24, 2017

Editorial Committee Members・Paper Committee Members

K. Kobayashi and T. Ono (Chairperson), T. Kato, K. Koike and T. Taniyama (Secretary)

A. Fujita	H. Goto	H. Hashino	S. Honda	S. Inui	Y. Kanai
S. Kasai	A. Kikitsu	H. Kikuchi	T. Kimura	T. Kubota	K. Miura
T. Nagahama	H. Naganuma	M. Naoe	M. Ohtake	N. Pham	Y. Sasayama
T. Sato	T. Sato	S. Seino	K. Sekiguchi	M. Sekino	T. Shima
Y. Shiratsuchi	M. Sonehara	T. Tanaka	K. Yamamoto	H. Yuasa	
N. Adachi	K. Bessho	M. Doi	T. Doi	M. Endo	T. Hasegawa
N. Inaba	S. Isogami	K. Kamata	H. Kato	K. Kato	T. Koda
S. Kokado	Y. Kota	T. Maki	E. Miyashita	T. Morita	S. Muroga
T. Nakagawa	H. Nakayama	T. Narita	D. Oyama	T. Saito	R. Sugita
K. Tajima	M. Takezawa	T. Takura	M. Tsunoda	S. Yabukami	T. Yamamoto
K. Yamazaki	S. Yoshimura				

Notice for Photocopying

If you wish to photocopy any work of this publication, you have to get permission from the following organization to which licensing of copyright clearance is delegated by the copyright owner.

〈All users except those in USA〉
Japan Academic Association for Copyright Clearance, Inc. (JAACC)
6–41 Akasaka 9-chome, Minato-ku, Tokyo 107–0052 Japan
Phone 81–3–3475–5618 FAX 81–3–3475–5619 E-mail: info@jaacc.jp

〈Users in USA〉
Copyright Clearance Center, Inc.
222 Rosewood Drive, Danvers, MA01923 USA
Phone 1–978–750–8400 FAX 1–978–646–8600

編集委員・論文委員

小林宏一郎（理事） 小野輝男（理事） 加藤剛志（幹事） 小池邦博（幹事） 谷山智康（幹事）

乾　成里	大竹　充	葛西伸哉	金井　靖	喜々津哲	菊池弘昭	木村　崇	窪田崇秀	後藤博樹
笹山瑛由	佐藤　拓	佐藤　岳	嶋　敏之	白土　優	清野智史	関口康爾	関野正樹	曽根原誠
田中哲郎	直江正幸	永沼　博	長浜太郎	橋野早人	PHAM NAMHAI		藤田麻哉	本多周太
三浦健司	山本健一	湯浅裕美						
安達信泰	磯上慎二	稲葉信幸	遠藤将起	小山大介	加藤宏朗	加藤和夫	鎌田清孝	神田哲典
古門聡士	小田洋平	齊藤敏明	杉田龍二	田倉哲也	竹澤昌晃	田島克文	角田匡清	土井達也
土井正晶	中川　貴	中山英俊	成田正敬	長谷川崇	別所和宏	槙　智仁	宮下英一	室賀　翔
森田　孝	薮上　信	山崎慶太	山本崇史	吉村　哲				

複写をされる方へ

本会は下記協会に複写に関する権利委託をしていますので，本誌に掲載された著作物を複写したい方は，同協会より許諾を受けて複写して下さい．但し（社）日本複写権センター（同協会より権利を再委託）と包括複写許諾契約を締結されている企業の社員による社内利用目的の複写はその必要はありません．（社外頒布用の複写は許諾が必要です．）

権利委託先：一般社団法人学術著作権協会
〒107–0052 東京都港区赤坂9–6–41 乃木坂ビル
電話（03）3475–5618 FAX（03）3475–5619 E-mail: info@jaacc.jp

なお，著作者の転載・翻訳のような，複写以外の許諾は，学術著作権協会では扱っていませんので，直接本会へご連絡ください．

本誌掲載記事の無断転載を禁じます．

Journal of the Magnetics Society of Japan

Vol. 41 No. 6 (通巻第 294 号) 2017 年 11 月 1 日発行

Vol. 41 No. 6 Published Nov. 1, 2017
by the Magnetics Society of Japan
Tokyo YWCA building Rm207, 1–8–11 Kanda surugadai, Chiyoda-ku, Tokyo 101–0062
Tel. +81–3–5281–0106 Fax. +81–3–5281–0107

Printed by JP Corporation Co., Ltd.
2–3–36, Minamikase, Saiwai-ku, Kanagawa 212–0055
Advertising agency: Kagaku Gijutsu-sha

発行：（公社）日本磁気学会 101–0062 東京都千代田区神田駿河台 1–8–11 東京YWCA会館 207 号室
製作：ジェイピーコーポレーション 212–0055 神奈川県川崎市幸区南加瀬 2–3–36 Tel.（044）571–5815
広告取扱い：科学技術社 111–0052 東京都台東区柳橋 2–10–8 武田ビル 4F Tel.（03）5809–1132

Copyright ©2017 by the Magnetics Society of Japan